Chapter 14

Algorithms for the Euler Equations in General Curvilinear Coordinates

14.1 Introduction

Here we will solve the Quasi 1-D Euler equations described in Section 7.5.1 for two initial value problems, (1) flow within a supersonic inlet, Figure 13.1, and (2) flow within a converging-diverging nozzle, Figure 13.11. These problems were chosen to illustrate algorithms and the application of boundary condition procedures, both explicit and implicit. The Euler equations in two dimensions written in Cartesian coordinates are

$$\frac{\partial U}{\partial t} + \frac{\partial F}{\partial x} + \frac{\partial G}{\partial y} = 0 \quad \text{where} \quad U = \begin{pmatrix} \rho \\ \rho u \\ \rho v \\ e \end{pmatrix}, \quad F = \begin{pmatrix} \rho u \\ \rho u^2 + p \\ \rho u v \\ (e+p)u \end{pmatrix}, \quad G = \begin{pmatrix} \rho v \\ \rho v u \\ \rho v^2 + p \\ (e+p)v \end{pmatrix}$$

$$\text{and} \quad p = (\gamma - 1)\rho\varepsilon, \quad \varepsilon = \frac{e}{\rho} - \frac{u^2 + v^2}{2}$$

14.2 Transformation to Curvilinear Coordinates

The Euler equations can be transformed into a general curvilinear coordinate system as follows (see also Sections 7.2- 3)

$$\frac{\partial U}{\partial t} + \frac{\partial F}{\partial x} + \frac{\partial G}{\partial y} = 0 \quad \Rightarrow \quad \frac{\partial U'}{\partial \tau} + \frac{\partial F'}{\partial \xi} + \frac{\partial G'}{\partial \eta} = 0$$

$$U' = \frac{1}{d_{\xi\eta}}U, \quad d_{\xi\eta} = \frac{\partial \xi}{\partial x}\frac{\partial \eta}{\partial y} - \frac{\partial \xi}{\partial y}\frac{\partial \eta}{\partial x}$$

$$F' = \frac{1}{d_{\xi\eta}}\left(F\frac{\partial \xi}{\partial x} + G\frac{\partial \xi}{\partial y} + U\frac{\partial \xi}{\partial t}\right) \quad and \quad G' = \frac{1}{d_{\xi\eta}}\left(F\frac{\partial \eta}{\partial x} + G\frac{\partial \eta}{\partial y} + U\frac{\partial \eta}{\partial t}\right)$$

Using the identities given earlier in Section 7.3,

$$U' = U \vee, \quad F' = F\frac{\partial y}{\partial \eta} - G\frac{\partial x}{\partial \eta} + U Q_\xi, \quad G' = -F\frac{\partial y}{\partial \xi} + G\frac{\partial x}{\partial \xi} + U Q_\eta$$

where the metric volume term V and reference frame velocities q_ξ and q_η are given by

$$\frac{1}{d_{\xi\eta}} = d_{xy} = V = \frac{\partial x}{\partial \xi}\frac{\partial y}{\partial \eta} - \frac{\partial x}{\partial \eta}\frac{\partial y}{\partial \xi}, \quad Q_\xi = \frac{\partial x}{\partial \eta}\frac{\partial y}{\partial \tau} - \frac{\partial y}{\partial \eta}\frac{\partial x}{\partial \tau}, \quad Q_\eta = \frac{\partial y}{\partial \xi}\frac{\partial x}{\partial \tau} - \frac{\partial x}{\partial \xi}\frac{\partial y}{\partial \tau} \quad and \quad \tau = t$$

The metric volume term V, often called J to represent the Jacobian of the coordinate transformation, is here represented in non-italic face to distinguish it from the vector V containing the primitive flow variables as elements.

14.2.1 Equations in Stationary Curvilinear Coordinates

Assuming the arbitrary coordinate system is stationary, i.e., $q_\xi = 0$, $q_\eta = 0$ and the volume V does not depend upon τ, the governing Euler equations can be written as

$$\frac{\partial U}{\partial t} + \frac{1}{V}\frac{\partial F'}{\partial \xi} + \frac{1}{V}\frac{\partial G'}{\partial \eta} = 0 \tag{14.1}$$

$$\text{where } F' = F\frac{\partial y}{\partial \eta} - G\frac{\partial x}{\partial \eta} \quad and \quad G' = -F\frac{\partial y}{\partial \xi} + G\frac{\partial x}{\partial \xi}$$

Note that the above equation, written in an arbitrary coordinate system, still retains its Cartesian roots in that the state vector U is still written in terms of the Cartesian velocities u and v. F' and G' represent rotated flux vectors, whose directions are orthogonal to the surfaces of constant ξ and η, respectively, though not necessarily orthogonal to each other.
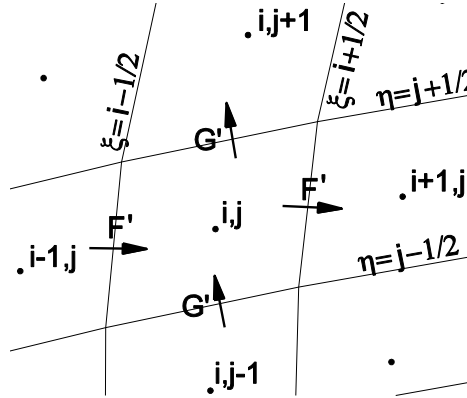

Figure 14.1 Computational coordinates induced from mesh point indices

14.2.1.1 Computational Coordinate System

Note that all spatial derivatives, of both the metric and flow variables, in the above equations are now taken with respect to ξ and η only. These variables will now become the computational coordinates in which the governing equations will be discretized and solved. For structured body fitted meshes, it is natural to use the indexing of the arrayed variables to induce the metric for the

2

computational coordinates. Therefore, at grid point i, j $\xi = i$ and $\eta = j$ and at flux surfaces between grid points ξ and η will take on half integer values, i.e., $\xi = i + 1/2$ and $\eta = j + 1/2$, as shown in the Figure 14.1. The distance between adjacent grid points in computational space is always $\Delta \xi = \Delta \eta = 1$ anywhere in the mesh. We will use this index induced metric from now on.

The metric term V now has the dimensions of volume. In two dimensions we assume unit depth in the third dimension. However, care should be taken regarding the new flux terms F' and G', whose dimensions differ from those of F and G by surface area factors.

14.2.1.2 Euler Flux Terms and Rotated Jacobians
The Euler flux vectors F' and G' can be represented as

$$F' = A'U \quad and \quad G' = B'U$$

where $A' = \dfrac{\partial y}{\partial n} A - \dfrac{\partial x}{\partial n} B, \quad B' = -\dfrac{\partial y}{\partial \xi} A + \dfrac{\partial x}{\partial \xi} B, \quad A = \dfrac{\partial F}{\partial U} \quad and \quad B = \dfrac{\partial G}{\partial U}$

Again, F' and G' represent rotated flux vectors. Similarly, A' and B' are rotated Jacobians. Caution should be maintained that they are dimensionally different from the Jacobians A and B in that they also have an added factor of surface area. They may be diagonalized as follows.

$$A' = S^{-1} R_{A'}^{-1} C_{A'}^{-1} \Lambda_{A'} C_{A'} R_{A'} S \quad and \quad B' = S^{-1} R_{B'}^{-1} C_{B'}^{-1} \Lambda_{B'} C_{B'} R_{B'} S$$

where S and S^{-1} are as given before in Section 9.4 and $C_{A'} = C_A$ and $C_{B'} = C_B$, which are also given in Section 9.6. $R_{A'}$ and $R_{B'}$ are rotation matrices with direction *cosine* elements.

$$R_{A'} = \begin{bmatrix} 1 & 0 & 0 & 0 \\ 0 & \cos\alpha & \sin\alpha & 0 \\ 0 & -\sin\alpha & \cos\alpha & 0 \\ 0 & 0 & 0 & 1 \end{bmatrix} \quad and \quad R_{A'}^{-1} = \begin{bmatrix} 1 & 0 & 0 & 0 \\ 0 & \cos\alpha & -\sin\alpha & 0 \\ 0 & \sin\alpha & \cos\alpha & 0 \\ 0 & 0 & 0 & 1 \end{bmatrix}$$

$$\text{where} \quad \cos\alpha = \frac{\dfrac{\partial y}{\partial \eta}}{\sqrt{\left(\dfrac{\partial x}{\partial \eta}\right)^2 + \left(\dfrac{\partial y}{\partial \eta}\right)^2}} \quad and \quad \sin\alpha = \frac{-\dfrac{\partial x}{\partial \eta}}{\sqrt{\left(\dfrac{\partial x}{\partial \eta}\right)^2 + \left(\dfrac{\partial y}{\partial \eta}\right)^2}},$$

$$R_{B'} = \begin{bmatrix} 1 & 0 & 0 & 0 \\ 0 & \cos\beta & -\sin\beta & 0 \\ 0 & \sin\beta & \cos\beta & 0 \\ 0 & 0 & 0 & 1 \end{bmatrix} \quad and \quad R_{B'}^{-1} = \begin{bmatrix} 1 & 0 & 0 & 0 \\ 0 & \cos\beta & \sin\beta & 0 \\ 0 & -\sin\beta & \cos\beta & 0 \\ 0 & 0 & 0 & 1 \end{bmatrix}$$

$$\text{where} \quad \cos\beta = \frac{\dfrac{\partial x}{\partial\xi}}{\sqrt{\left(\dfrac{\partial x}{\partial\xi}\right)^2 + \left(\dfrac{\partial y}{\partial\xi}\right)^2}} \quad \text{and} \quad \sin\beta = \frac{-\dfrac{\partial y}{\partial\xi}}{\sqrt{\left(\dfrac{\partial x}{\partial\xi}\right)^2 + \left(\dfrac{\partial y}{\partial\xi}\right)^2}}$$

The diagonal matrices $\Lambda_{A'}$ and $\Lambda_{B'}$ are given by

$$\Lambda_{A'} = d_{A'}\begin{bmatrix} u' & 0 & 0 & 0 \\ 0 & u'+c & 0 & 0 \\ 0 & 0 & u' & 0 \\ 0 & 0 & 0 & u'-c \end{bmatrix}, \quad \Lambda_{B'} = d_{B'}\begin{bmatrix} v' & 0 & 0 & 0 \\ 0 & v' & 0 & 0 \\ 0 & 0 & v'+c & 0 \\ 0 & 0 & 0 & v'-c \end{bmatrix}$$

$$\text{where} \quad d_{A'} = \sqrt{\left(\frac{\partial x}{\partial\eta}\right)^2 + \left(\frac{\partial y}{\partial\eta}\right)^2}, \quad d_{B'} = \sqrt{\left(\frac{\partial x}{\partial\xi}\right)^2 + \left(\frac{\partial y}{\partial\xi}\right)^2}$$

$$u' = \cos\alpha\, u + \sin\alpha\, v \quad \text{and} \quad v' = \sin\beta\, u + \cos\beta\, v$$

The additional factor of surface area is evident in the definitions of the diagonal matrices $\Lambda_{A'}$ and $\Lambda_{B'}$ by comparison with those defined previously in Section 9.4.

14.2.1.3 Flux Vectors for the Steger-Warming, Modified-Steger-Warming and Roe Methods
For the general curvilinear coordinate system, we can define, as in Section 9.11, the following F' flux vectors for the Steger-Warming, Modified-Steger-Warming (Version 1) and Roe Methods as follows

$$F'^{(S-W)}_{i+1/2} = A'_{+_L} U_L + A'_{-_R} U_R$$

$$F'^{(M-S-W-I)}_{i+1/2} = \overline{A}'_{+_{i+1/2}} U_L + \overline{A}'_{-_{i+1/2}} U_R$$

$$F'^{(M-S-W-II)}_{i+1/2} = \overline{\mathcal{A}}'_{+_{i+1/2}} F'_L + \overline{\mathcal{A}}'_{-_{i+1/2}} F'_R$$

$$F'^{(Roe)}_{i+1/2} = \frac{F'_L + F'_R}{2} - \frac{1}{2}\left|\hat{A}'_{i+1/2}\right|\left(U_R - U_L\right)$$

The G' flux vectors are similarly defined. Note that in this arbitrary coordinate system, with rotated flux vectors, the actual direction with respect to the Cartesian x and y coordinate directions becomes unimportant. An F' flux vector can be rotated 360° and has little distinction from a G' flux vector. They differ only the choice of mesh points used to define the flow variables and metric terms. For this reason a single subroutine can and be written to define both, as long as the mesh point indices related to the surface at which the flux is to be calculated are used correctly.

4

14.2.1.4 The Generic Difference Equations in Stationary Curvilinear Coordinates

The Generic Explicit Difference Equation

The *generic explicit difference equation* for both the finite difference and volume approaches for solving Equation 14.1 can be written as follows.

$$U_{i,j}^{n+1} = U_{i,j}^n - \frac{\Delta t}{V_{i,j}}\left(\frac{F_{i+1/2,j}''^n - F_{i-1/2,j}''^n}{\Delta \xi} + \frac{G_{i,j+1/2}''^n - G_{i,j-1/2}''^n}{\Delta \eta} \right)$$

The Generic Implicit Difference Equation

The *generic implicit difference equation* for both the finite difference and volume approaches for solving Equation 14.1 can be written as follows.

$$\left\{ I + \alpha \frac{\Delta t}{V_{i,j}}\left(\frac{D_-\cdot}{\Delta \xi}\bar{A}_{+i+1/2,j}''^n + \frac{D_+\cdot}{\Delta \xi}\bar{A}_{-i-1/2,j}''^n + \frac{D_-\cdot}{\Delta \eta}\bar{B}_{+i,j+1/2}''^n + \frac{D_+\cdot}{\Delta \eta}\bar{B}_{-i,j-1/2}''^n \right) \right\}\delta U_{i,j}^{n+1} = \Delta U_{i,j}^n$$

$$= -\frac{\Delta t}{V_{i,j}}\left(\frac{F_{i+1/2,j}''^n - F_{i-1/2,j}''^n}{\Delta \xi} + \frac{G_{i,j+1/2}''^n - G_{i,j-1/2}''^n}{\Delta \eta} \right)$$

where $\alpha = 1$, for first order flux approximations and $\alpha \geq 3/2$, for higher order flux approximations. Again, the two dimensional implicit equation represents a pentadiagonal block element matrix equation, as shown below.

$$\bar{B}_{i,j}\delta U_{i,j+1}^{n+1} + \bar{A}_{i,j}\delta U_{i,j}^{n+1} + \bar{C}_{i,j}\delta U_{i,j-1}^{n+1} + \bar{D}_{i,j}\delta U_{i+1,j}^{n+1} + \bar{E}_{i,j}\delta U_{i-1,j}^{n+1} = \Delta U_{i,j}^n$$

$$= -\frac{\Delta t}{V_{i,j}}\left(\frac{F_{i+1/2,j}''^n - F_{i-1/2,j}''^n}{\Delta \xi} + \frac{G_{i,j+1/2}''^n - G_{i,j-1/2}''^n}{\Delta \eta} \right)$$

The block element matrices $\bar{A}_{i,j}$, $\bar{B}_{i,j}$, $\bar{C}_{i,j}$, $\bar{D}_{i,j}$ and $\bar{E}_{i,j}$ are defined as follows.

$$\bar{A}_{i,j} = I + \alpha \frac{\Delta t}{V_{i,j}\Delta \xi}\left(\bar{A}_{+i+1/2,j}''^n - \bar{A}_{-i-1/2,j}''^n \right) + \alpha \frac{\Delta t}{V_{i,j}\Delta \eta}\left(\bar{B}_{+i,j+1/2}''^n - \bar{B}_{-i,j-1/2}''^n \right),$$

$$\bar{B}_{i,j} = +\alpha \frac{\Delta t}{V_{i,j}\Delta \eta}\bar{B}_{-i,j+1/2}''^n, \qquad \bar{C}_{i,j} = -\alpha \frac{\Delta t}{V_{i,j}\Delta \eta}\bar{B}_{+i,j-1/2}''^n,$$

$$\bar{D}_{i,j} = +\alpha \frac{\Delta t}{V_{i,j}\Delta \xi}\bar{A}_{-i+1/2,j}''^n \qquad and \qquad \bar{E}_{i,j} = -\alpha \frac{\Delta t}{V_{i,j}\Delta \xi}\bar{A}_{+i-1/2,j}''^n$$

Procedures for solving implicit matrix equations are given in Chap.11

14.2.2 The Non-Stationary Coordinate Transformation Case

Assuming the motion of the arbitrary coordinate system is known as a function of time, $t = \tau$, the governing Euler Equations can be written as

$$\frac{\partial U'}{\partial t} + \frac{\partial F'}{\partial \xi} + \frac{\partial G'}{\partial \eta} = 0 \qquad (14.2)$$

with $U' = U V$, $F' = F \dfrac{\partial y}{\partial \eta} - G \dfrac{\partial x}{\partial \eta} + U Q_\xi$, $G' = -F \dfrac{\partial y}{\partial \xi} + G \dfrac{\partial x}{\partial \xi} + U Q_\eta$

$$V = \frac{\partial x}{\partial \xi} \frac{\partial y}{\partial \eta} - \frac{\partial x}{\partial \eta} \frac{\partial y}{\partial \xi}, \quad Q_\xi = \frac{\partial x}{\partial \eta} \frac{\partial y}{\partial \tau} - \frac{\partial y}{\partial \eta} \frac{\partial x}{\partial \tau}, \quad Q_\eta = \frac{\partial y}{\partial \xi} \frac{\partial x}{\partial \tau} - \frac{\partial x}{\partial \xi} \frac{\partial y}{\partial \tau}$$

The volume V is in general now a function of time, because the computational coordinates ξ and η may be stretching or deforming with respect to the physical $x - y$ space. Therefore, the volume V can not be removed from the time derivative term as before. The $\xi - \eta$ coordinate space may be attached to a moving surface along a boundary of the flow field or a feature, such as a shock wave, within the flow. The computational coordinate system, described in Section 14.2.1.1, still applies to the present moving coordinate system case. The Euler flux vectors F' and G' now include terms representing the additional flux caused by the coordinate surfaces moving through the fluid as well as the previous terms representing the fluid moving through the physical coordinate system. The rotated Jacobians presented earlier need to be modified to include these additional terms.

$$A' = \frac{\partial y}{\partial n} A - \frac{\partial x}{\partial n} B + Q_\xi I \quad and \quad B' = -\frac{\partial y}{\partial \xi} A + \frac{\partial x}{\partial \xi} B + Q_\eta I$$

The matrices S, $C_{A'}$, $C_{B'}$, $R_{A'}$, $R_{B'}$, $\Lambda_{A'}$ and $\Lambda_{B'}$ are as defined before. But the flux velocities u' and v' need to be modified as follows.

$$u' = \cos\alpha\, u + \sin\alpha\, v + q_\xi \quad and \quad v' = \sin\beta\, u + \cos\beta\, v + q_\eta$$

with $\qquad q_\xi = Q_\xi / d_{A'} \qquad and \qquad q_\eta = Q_\eta / d_{B'}$

14.2.2.1 The Generic Explicit Difference Equation

The *generic explicit difference equation* for both the finite difference and volume approaches for solving Equation 14.2 becomes for the moving computational coordinate system.

$$U_{i,j}^{n+1} V_{i,j}^{n+1} = U_{i,j}^{n} V_{i,j}^{n} - \Delta t \left(\frac{F_{i+1/2,j}'^{n} - F_{i-1/2,j}'^{n}}{\Delta \xi} + \frac{G_{i,j+1/2}'^{n} - G_{i,j-1/2}'^{n}}{\Delta \eta} \right)$$

14.2.2.2 The Generic Implicit Difference Equation

The *generic implicit difference equation* for both the finite difference and volume approaches for solving Equation 14.2 becomes.

$$\left\{ I + \alpha \Delta t \left(\frac{D_- \cdot}{\Delta \xi} \bar{A}'^n_{+i+1/2,j} + \frac{D_+ \cdot}{\Delta \xi} \bar{A}'^n_{-i-1/2,j} + \frac{D_- \cdot}{\Delta \eta} \bar{B}'^n_{+i,j+1/2} + \frac{D_+ \cdot}{\Delta \eta} \bar{B}'^n_{-i,j-1/2} \right) \frac{1}{V^{n+1}_{i,j}} \right\} \delta U'^{n+1}_{i,j} = \Delta U'^n_{i,j}$$

$$= -\Delta t \left(\frac{F''^n_{i+1/2,j} - F''^n_{i-1/2,j}}{\Delta \xi} + \frac{G''^n_{i,j+1/2} - G''^n_{i,j-1/2}}{\Delta \eta} \right)$$

Notice the prime on $\delta U'^{n+1}_{i,j}$ indicating that $\delta U'^{n+1}_{i,j} = U'^{n+1}_{i,j} - U'^n_{i,j} = U^{n+1}_{i,j} V^{n+1}_{i,j} - U^n_{i,j} V^n_{i,j}$ and that the double primed $F''^n_{i+1/2,j}$ and $G''^n_{i,j+1/2}$ are defined as

$$F''^n_{i+1/2,j} = F'^n_{i+1/2,j} V^n_{i+1/2,j} / V^{n+1}_{i+1/2,j} \text{ and } G''^n_{i,j+1/2} = G'^n_{i,j+1/2} V^n_{i,j+1/2} / V^{n+1}_{i,j+1/2}$$

However, A', B' and their split jacobian matrices are defined as above.

Again $\alpha = 1$, for first order flux approximations and $\alpha \geq 3/2$, for higher order flux approximations. Again, the two dimensional implicit equation represents a pentadiagonal block element matrix equation, as shown below.

$$\bar{B}_{i,j} \delta U'^{n+1}_{i,j+1} + \bar{A}_{i,j} \delta U'^{n+1}_{i,j} + \bar{C}_{i,j} \delta U'^{n+1}_{i,j-1} + \bar{D}_{i,j} \delta U'^{n+1}_{i+1,j} + \bar{E}_{i,j} \delta U'^{n+1}_{i-1,j} = \Delta U'^n_{i,j}$$

$$= -\Delta t \left(\frac{F''^n_{i+1/2,j} - F''^n_{i-1/2,j}}{\Delta \xi} + \frac{G''^n_{i,j+1/2} - G''^n_{i,j-1/2}}{\Delta \eta} \right)$$

The block element matrices $\bar{A}_{i,j}$, $\bar{B}_{i,j}$, $\bar{C}_{i,j}$, $\bar{D}_{i,j}$ and $\bar{E}_{i,j}$ are defined as follows.

$$\bar{A}_{i,j} = I + \alpha \frac{\Delta t}{V_{i,j} \Delta \xi} \left(\bar{A}'^n_{+i+1/2,j} - \bar{A}'^n_{-i-1/2,j} \right) + \alpha \frac{\Delta t}{V_{i,j} \Delta \eta} \left(\bar{B}'^n_{+i,j+1/2} - \bar{B}'^n_{-i,j-1/2} \right),$$

$$\bar{B}_{i,j} = +\alpha \frac{\Delta t}{V_{i,j+1} \Delta \eta} \bar{B}'^n_{-i,j+1/2}, \qquad \bar{C}_{i,j} = -\alpha \frac{\Delta t}{V_{i,j-1} \Delta \eta} \bar{B}'^n_{+i,j-1/2},$$

$$\bar{D}_{i,j} = +\alpha \frac{\Delta t}{V_{i+1,j} \Delta \xi} \bar{A}'^n_{-i+1/2,j} \qquad and \qquad \bar{E}_{i,j} = -\alpha \frac{\Delta t}{V_{i-1,j} \Delta \xi} \bar{A}'^n_{+i-1/2,j}$$

Procedures for solving this implicit matrix equation are given in Chapter 11.

14.3 Two Dimensional Applications
14.3.1 Flow Past a Wedge
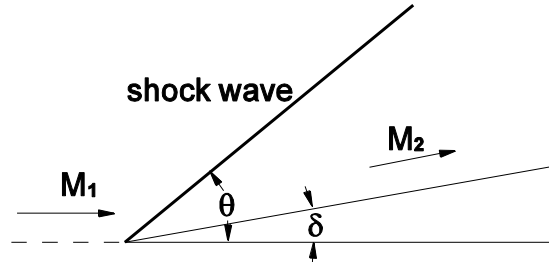
Figure 14.2 Flow past a wedge

Exercise(1): Solve the two dimensional Euler equations for supersonic flow past a wedge. The wedge angle $\delta = 10^o$ and the Mach number is $M_\infty = M_1 = 2$
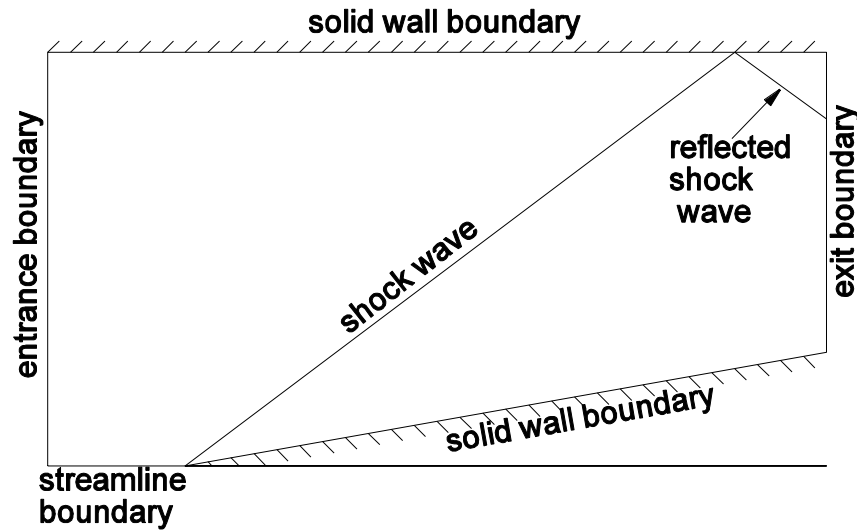

Figure 14.3 Sketch of flow field

Numerical Methods:
Start with the MacCormack method and then choose either the Modified Steger Warming or the Roe method. See Chapter 12 for the entrance, exit solid wall and streamline boundary conditions.

Initial Conditions:
At $t = t_0$, $p = 10^5 N/m^2$, $\text{T} = 300^o K$, $u = M_\infty c$ *and* $v = 0$ everywhere, and c is the speed of sound. The flow will converge to a steady state asymptotically in time.

Case (1) Mesh:
The mesh shown below uses 36x20 mesh volumes to cover the flow field including a border of "ghost" volumes, not shown, to be used for boundary conditions. The mesh could also be considered as a finite difference mesh of 35x19 points. The flow volume is 1.8m. high at the entrance and is 2.8m. long. The origin is located at the wedge tip, 0.6m from the entrance boundary. The mesh is equally spaced in the x-direction and is equally spaced at each x location in the y-direction.
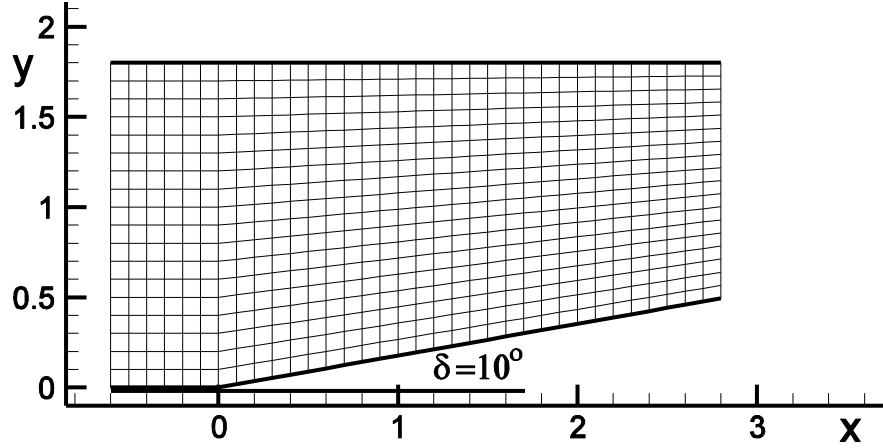
Figure 14.4 Case (1) mesh, 36x20 mesh volumes

Case (2) Mesh:

The Case (2) mesh is swept back to align the grid line starting at the wedge tip with the shock wave. See Section 2.4.3.6 to review the theory of an oblique shock wave attached to the tip of a wedge, partly repeated below.

Shock jump relations
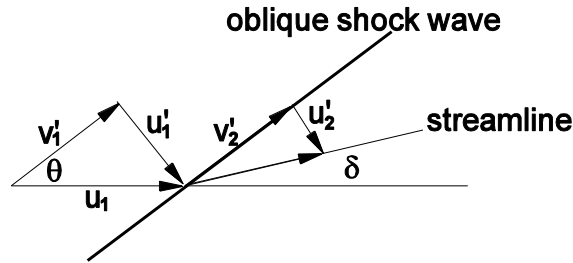
Figure 14.5 Velocity components

The oblique shock relations for the steady Euler equations are as follows.

$$(1) \ \rho_2 u_2' = \rho_1 u_1' = m$$

$$(2) \ \rho_2 u_2'^2 + p_2 = \rho_1 u_1'^2 + p_1 = n$$

$$(3) \ \rho_2 u_2' v_2' = \rho_1 u_1' v_1'$$

$$(4) \ (e_2 + p_2)u_2' = (e_1 + p_1)u_1'$$

where

$$u' = u\sin\theta - v\cos\theta$$
$$v' = u\cos\theta + v\sin\theta$$

The subscript 1 refers to the flow ahead of the shock wave and 2 to post shock conditions. Relation (3) simplifies to $v_2' = v_1'$ (3') and relation (4) becomes $\dfrac{e_2 + p_2}{\rho_2} = \dfrac{e_1 + p_1}{\rho_1} = h$ or

9

$\dfrac{\gamma}{\gamma-1}\dfrac{p_2}{\rho_2}+\dfrac{1}{2}(u'^2_2+v'^2_2)=h$ (4'). The quantities m, n, u'_1, v'_1 and h are known functions of θ and the flow conditions ahead of the shock wave (i.e., $u'_1=u_1\sin\theta$, $v'_1=u_1\cos\theta$) . There are 5 unknowns ρ_2, u'_2, v'_2, p_2 and θ and 4 relations. A fifth relation is known from the flow behind the shock wave that moves parallel to the wedge surface, $\dfrac{v'_2}{u'_2}=\tan(\theta-\delta)$ or $u'_2=\dfrac{v'_1}{\tan(\theta-\delta)}$. A single equation can be formed by substitution of equations (1) , (2) and (3') into equation (4').

$$f(\theta)=\frac{\gamma}{\gamma-1}\frac{n}{m}u'_2+\left(\frac{1}{2}-\frac{\gamma}{\gamma-1}\right)u'^2_2+\frac{1}{2}v'^2_1-h=0$$

Newton's method can be used to find the values of θ for which $f(\theta)=0$ as shown in Section 5.3.1. There can be two such solutions for a given free stream Mach number and wedge angle δ, the preferred weak shock solution and the strong shock wave solution. In our case, $\theta=39.31^o$ is the weak shock solution and $\theta=83.70^o$ is the strong shock solution. A mesh, swept back to align the mesh with the oblique shock wave, is shown in Figure 14.6, now containing 30x20 mesh volumes.
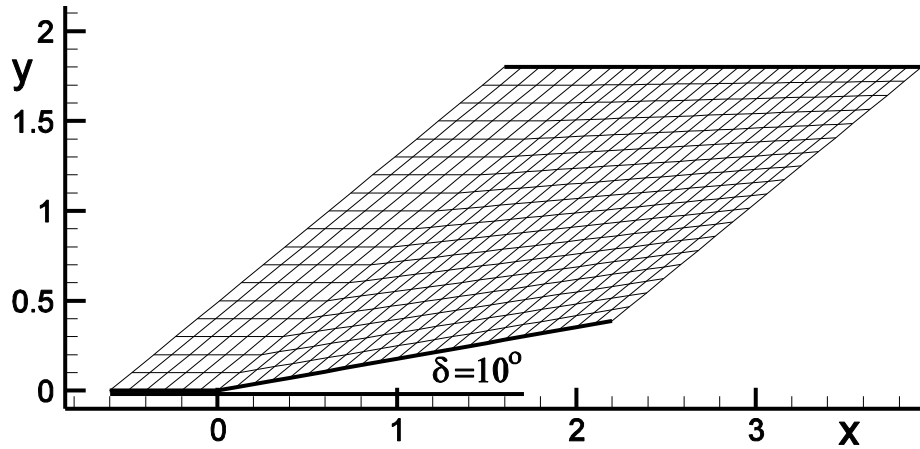
Figure 14.6 Case (2) swept mesh, 30x20 mesh volumes

Algorithms:
Use the generic form of the difference equations

$$U^{n+1}_{i,j}=U^n_{i,j}-\frac{\Delta t}{V_{i,j}}\left(\frac{F^m_{i+1/2,j}-F^m_{i-1/2,j}}{\Delta\xi}+\frac{G^m_{i,j+1/2}-G^m_{i,j-1/2}}{\Delta\eta}\right)$$

where the $F' = \vec{F} \cdot \vec{S} = F \dfrac{\partial y}{\partial \eta} - G \dfrac{\partial x}{\partial \eta}$ is given below for several methods by, (see also Chapter 9 for other methods)

$$F''^{n}_{i+1/2,j} = \vec{F}^{n}_{i+1/2,j} \cdot \vec{S}_{i+1/2} = \begin{cases} F''^{n}_{ii,j}, \quad ii = \begin{cases} i, & backward\ difference \\ i+1, & forward\ difference \end{cases} \quad \text{MacCormack} \\ A'^{n}_{+i,j} U^{n}_{i,j} + A'^{n}_{-i+1,j} U^{n}_{i+1,j}, \qquad\qquad \text{Steger} - \text{Warming} \\ \bar{A}'^{n}_{+i+1/2,j} U^{n}_{i,j} + \bar{A}'^{n}_{-i+1/2,j} U^{n}_{i+1,j}, \quad \text{Modified Steger} - \text{Warming (1)} \\ \mathcal{A}'^{n}_{+i+1/2,j} F'_{i,j} + \mathcal{A}'^{n}_{-i+1/2,j} F'_{i+1,j}, \quad \text{Modified Steger} - \text{Warming (2)} \\ \dfrac{F''^{n}_{i,j} + F''^{n}_{i+1,j}}{2} - \dfrac{1}{2}\left|\hat{A}'^{n}_{i+1/2,j}\right|\left(U^{n}_{i+1,j} - U^{n}_{i,j}\right) \qquad \text{Roe} \end{cases}$$

$$F'_{i+1/2,j} = \vec{F}_{i+1/2,j} \cdot \vec{S}_{i+1/2} = \left(F_{i+1/2,j}\ \vec{i}_x + G_{i+1/2,j}\ \vec{i}_y\right) \cdot \left(sx_{i+1/2}\ \vec{i}_x + sy_{i+1/2}\ \vec{i}_y\right) = \begin{pmatrix} \rho u' \\ \rho u u' + sx\,p \\ \rho v u' + sy\,p \\ (e+p)u' \end{pmatrix}_{i+1/2,j}$$
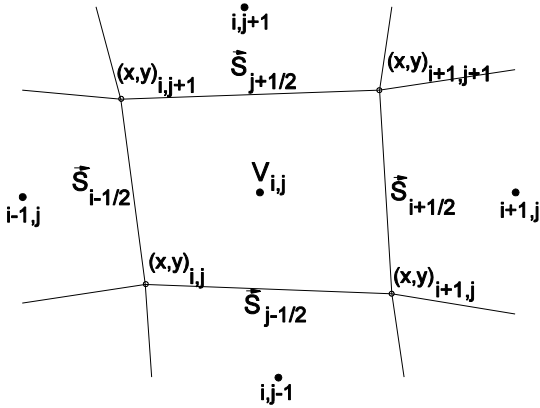
Figure 14.7 Arbitrary mesh volume

$$\vec{S}_{i+1/2} = \dfrac{\partial y}{\partial \eta}\Delta\eta\bigg|_{\xi=i+1/2} \vec{i}_x - \dfrac{\partial x}{\partial \eta}\Delta\eta\bigg|_{\xi=i+1/2} \vec{i}_y$$

$$= +(y_{i+1,j+1} - y_{i+1,j})\vec{i}_x - (x_{i+1,j+1} - x_{i+1,j})\vec{i}_y$$

$$\vec{S}_{j+1/2} = -\dfrac{\partial y}{\partial \xi}\Delta\eta\xi\bigg|_{\eta=j+1/2} \vec{i}_x + \dfrac{\partial x}{\partial \xi}\Delta\xi\bigg|_{\eta=j+1/2} \vec{i}_y$$

$$= -(y_{i+1,j+1} - y_{i,j+1})\vec{i}_x + (x_{i+1,j+1} - x_{i,j+1})\vec{i}_y$$

The mesh volume can be calculated by

$$V_{i,j} = \dfrac{1}{2}\{\left|(x_{i,j} - x_{i+1,j})y_{i+1,j+1} + (x_{i+1,j} - x_{i+1,j+1})y_{i,j} + (x_{i+1,j+1} - x_{i,j})y_{i+1,j}\right|$$

$$+ \left|(x_{i,j} - x_{i+1,j+1})y_{i,j+1} + (x_{i+1,j+1} - x_{i,j+1})y_{i,j} + (x_{i,j+1} - x_{i,j})y_{i+1,j+1}\right|\}$$

Time Step:
The time step limit can be expressed on a Cartesian mesh as

$$\Delta t \le \min_{i,j} \left\{ \frac{1}{\dfrac{|u_{i,j}|}{\Delta x_{i,j}} + \dfrac{|v_{i,j}|}{\Delta y_{i,j}} + c_{i,j}\sqrt{\dfrac{1}{\Delta x_{i,j}^2} + \dfrac{1}{\Delta y_{i,j}^2}}} \right\} = \Delta t_{\max}$$

On an arbitrary curvilinear mesh

$$\Delta t \le \min_{i,j} \left\{ \frac{V_{i,j}}{\left|\vec{q}_{i,j} \cdot \vec{S}_{i+1/2}\right| + \left|\vec{q}_{i,j} \cdot \vec{S}_{j+1/2}\right| + c_{i,j}\sqrt{\left|\vec{S}_{i+1/2} \cdot \vec{S}_{i+1/2}\right| + \left\|\vec{S}_{j+1/2} \cdot \vec{S}_{j+1/2}\right\|}} \right\} = \Delta t_{\max}$$

where the velocity $\vec{q} = u\vec{i}_x + v\vec{i}_y$. To be safe, the time step should be chosen to be less than $\Delta t_{\max}$. For example, $\Delta t = cfl \cdot \Delta t_{\max}$, where the factor $cfl \simeq 0.9 \ or \ 0.8$.

Wedge Solutions:
Run your program until convergence, about 250 time steps, for each case.

For Mach two flow past a wedge with $\delta = 10^o$, the oblique shock wave angle is 39.31^o and the pressure ratio at across the shock is $\dfrac{p_2}{p_1} = 1.71$.
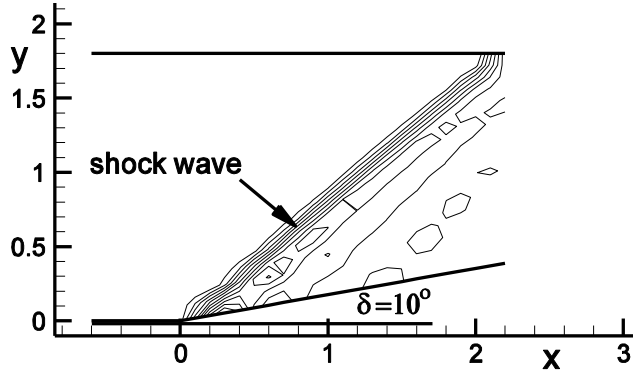
Figure 14.8 Case (1) mesh pressure contours   Case (2) swept mesh pressure contours
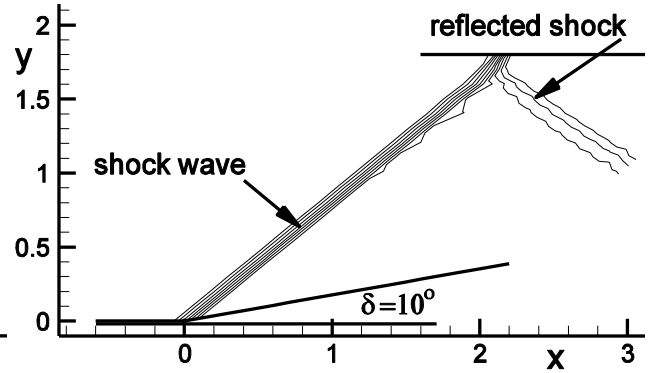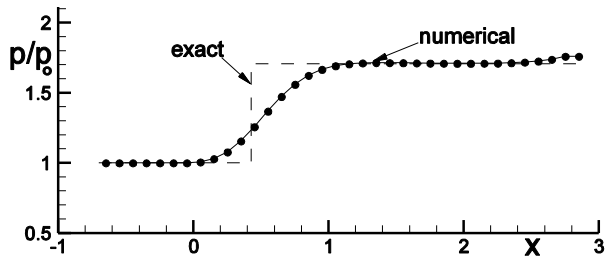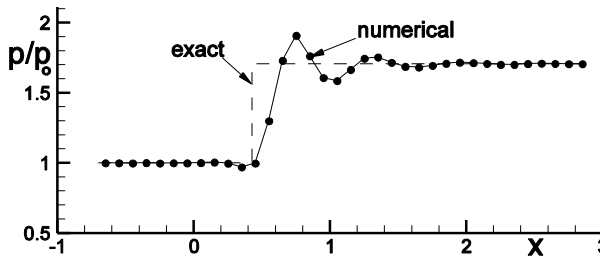
Figure 14.9 Case (1) results, pressure, at left MacCormack method and at right Roe method
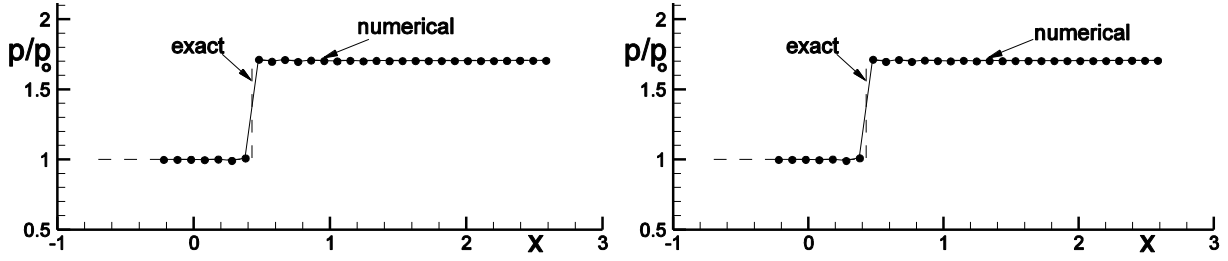
Figure 14.10 Case (2) results, pressure, at left MacCormack method and at right Roe method

Figure 14.8 shows the improvement in the solution obtained by aligning the mesh with the shock wave. The exact and computed pressures are compared for both meshes in Figures 14.9 and 14.10, through the shock wave along $j = 5$ for both the MacCormack method and the first order accurate Roe method.

Case (3) adaptive mesh shock alignment

Start with the unaligned mesh of case (1) and adapt the mesh to align with the forming shock wave similar to the procedure used in Section 13.4, where the following formula was derived in terms of conditions on either side of the shock wave.

$$\sin \theta = \sqrt{\frac{\gamma p_2}{\rho_1 u_1^2} + \frac{\gamma - 1}{2 \rho_1 u_1^2}(p_2 - p_1)}$$

The grid line passing through the corner point of the mesh is designated $i = i_{cnr}$. This line, initially the vertical line starting at the apex of the wedge, is chosen to align itself with the shock wave. For the finite volume mesh, line $j = 2$ runs along the wedge surface and along y=0 ahead of the wedge and line $j = J$ runs along the top boundary. After each time strep the mesh is adapted as follows.

First the new position of the mesh line $i = i_{cnr}$ is determined

For $j = 2$ to J

$$\sin \theta_j = \sqrt{\frac{\gamma p_{i_{cnr},j}}{\rho_\infty u_\infty^2} + \frac{\gamma - 1}{2 \rho_\infty u_\infty^2}(p_{i_{cnr},j} - p_\infty)}$$

$$\theta_j = \sin^{-1}(\sin \theta_j)$$

$$x_{i_{cnr},j+1} = x_{i_{cnr},j} + (y_{i_{cnr},j+1} - y_{i_{cnr},j})/\tan \theta_j$$

Then the entire mesh is aligned with the new position of the mesh line i=icnr
For $i = 1$ to I and $j = 3$ to J

$$x_{i,j+1} = x_{i,j} + (y_{i,j+1} - y_{i,j})/\tan \theta_j$$

13

For this simple supersonic flow, the mesh will sweep back on the first time step into alignment with a Mach wave, $\theta_j = \sin^{-1}(1/M_\infty)$, but on succeeding steps it will align itself with the forming shock wave. Figure shows the results after about 250 time steps for the Modified-Steger-Warming, Version (2) algorithm. The mesh is nicely aligned with the shock wave and the pressure through the shock wave along $j = 5$ is fairly sharp at the shock.
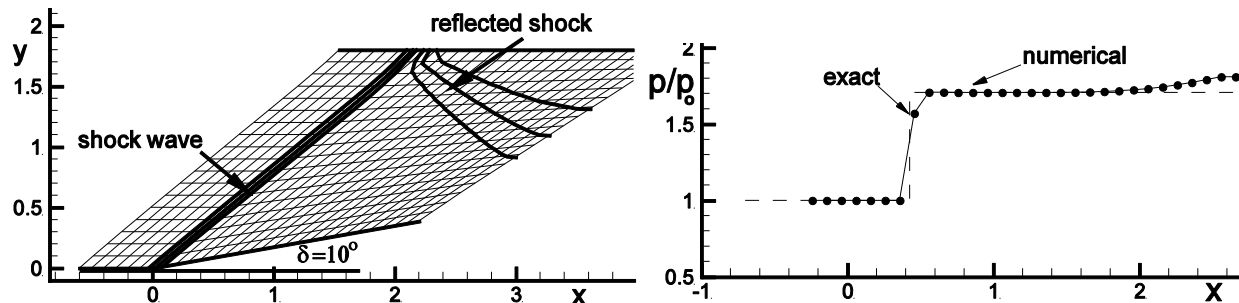
Figure 14.11 Case (3) results for the Modified-Steger-Warming, Version (2) algorithm

14.3.2 Flow Past a Circular Arc Airfoil

Exercise(2): Solve the Euler equations for Case (1) subsonic flow at $M_\infty = 0.735$ and Case (2) transonic flow at $M_\infty = 0.908$ past a 6% thick circular arc airfoil of chord length $c = 1$ on a 51×51 mesh, with 21 equally spaced points over the airfoil and stretched to far field boundaries 50 chord lengths away. Start with the explicit first order accurate Modified Steger-Warming Flux Vector Split method. Then try the Roe Flux Difference Vector Split method and the pure Steger-Warming method.
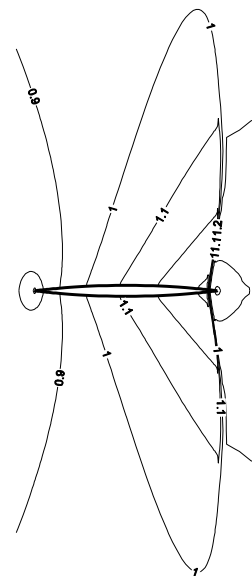
Figure 14.12 Mach contours

Solution Approach: We could use non-dimensional units, but for this case let's use metric units and assume that $c = 1m$ and that the flow has a total pressure and temperature near atmospheric, $p_t = 1.0 \times 10^5 \, N/m^2$ and $T_t = 300^o K$. The figure below shows a schematic of the flow field. The left and right boundaries are entrance and exit subsonic boundaries (see Sections 12.4 and 12.5) and the top and bottom are streamline boundaries. Streamline boundaries are impermeable boundaries and can represent solid walls for inviscid flow (see Section 12.2).
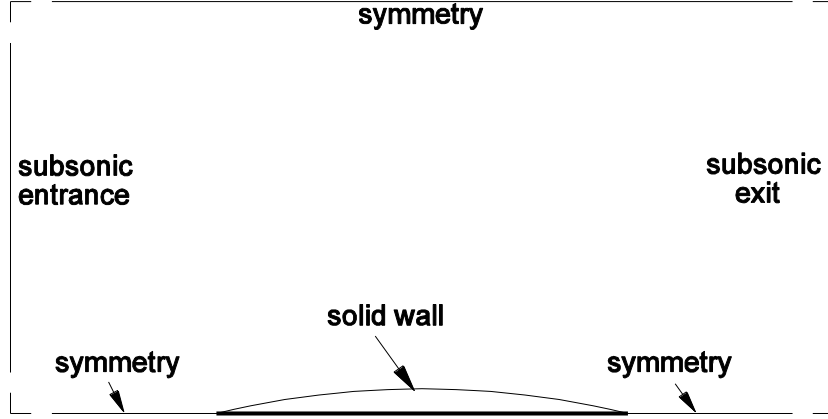
Figure 14.13 Flow volume about symmetric circular arc airfoil

Mesh

A mesh similar to that shown in Section 5.3 (see Figure 5.10), but fitted along the body surface, is shown in the figure below. This mesh was formed using the same stretching formula as in Section 5.3, $y_j = y_1 + D\dfrac{e^{\kappa\frac{j-1}{JL-1}} - 1}{e^\kappa - 1}$, where $JL = 51$ and $D = 50c$. Newton's method was used to find κ. This formula was then modified, using the same κ for the body fitted mesh, as follows.

$$y_{i,j} = y_{i,2} + (D - y_{i,2})\frac{e^{\kappa\frac{j-2}{JL-2}} - 1}{e^\kappa - 1}, \quad j = 2, \cdots, JL$$

The points $y_{i,2}$ lie along the lower boundary and over the airfoil surface. We could have chosen $y_{i,1}$ for the lower boundary points, but this choice will allow space for boundary conditions for the *finite volume* approach. Mesh points at $j = 1$ are obtained by reflection

$$x_{i,1} = 2x_{i,2} - x_{i,3} \text{ and } y_{i,1} = 2y_{i,2} - y_{i,3}$$

Similarly, an additional mesh point at the top of the mesh is can be obtained by

$$x_{i,JL+1} = 2x_{i,JL} - x_{i,JL-1} \text{ and } y_{i,JL+1} = 2y_{i,JL} - y_{i,JL-1}$$

This extension of the mesh is strictly not needed for the *finite difference* approach, but maybe useful there as well. The mesh for both approaches is shown below near the airfoil. The *finite difference* approach locates mesh points at the intersections of the mesh lines, placing points along boundary surfaces. The *finite volume* approach locates mesh points at the centers of volumes formed by the mesh lines (surfaces in 3D) and places volume surfaces along boundaries. The *finite volume* method uses one more point in each direction than the *finite difference* method. For example, the finite difference approach will use 51 mesh points to span the flow from the airfoils surface to the top boundary, including two boundary points. The finite volume will span this distance with 50 volumes

plus two "ghost" volumes along and across the boundaries. The ghost volumes are not shown in the mesh below.
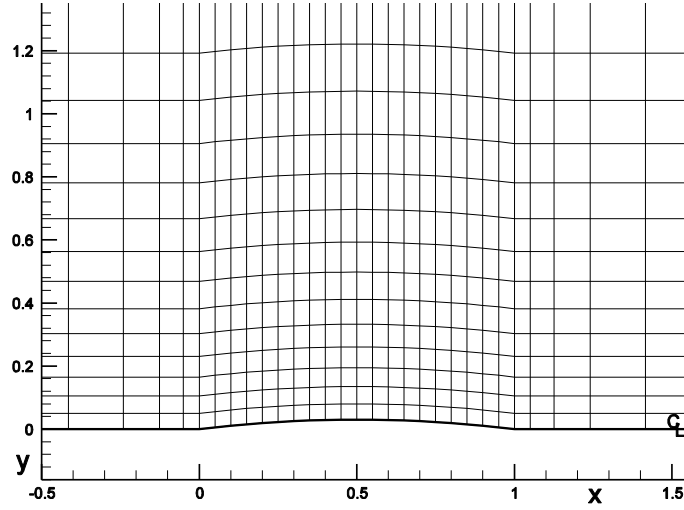
Figure 14.14 Mesh near airfoil.

As shown in the mesh $\Delta y_{\min} = c / 20$, which is considerably larger than that used for solving the Transonic Small Disturbance equation in Chap.5. This choice is made because we will solve the Euler equations explicitly, and the time step size would then be too small for solutions to be obtained within a few hundred iterations. Later we will remove the time step restriction by using fully implicit methods.

Initial Conditions
Given the Mach number, we can use isentropic relations to find initial values for the flow variables.

$$T^0_{i,j} = T_\infty = T_t \left[1 + \frac{\gamma - 1}{2} M_\infty^2\right]^{-1}$$

$$p^0_{i,j} = p_\infty = p_t \left[1 + \frac{\gamma - 1}{2} M_\infty^2\right]^{-\frac{\gamma}{\gamma - 1}}$$

and therefore $\rho^0_{i,j} = \rho_\infty = \dfrac{p_\infty}{(\gamma - 1)c_v T_\infty}$, $c^0_{i,j} = c_\infty = \sqrt{\dfrac{\gamma p_\infty}{\rho_\infty}}$, $u^0_{i,j} = u_\infty = c_\infty M_\infty$ and $v^0_{i,j} = 0$

Boundary Conditions
The symmetry boundaries are streamlines of the flow, as is the solid wall section of the airfoil. These boundaries are impermeable and flow tangency requires that the normal component of velocity is zero. Section 12.2 shows that "all you need is p" at these boundaries and presents relations for obtaining pressure along impermeable boundaries. The subsonic entrance and exit boundaries condition procedures are found in Sections 12.4 and 12.5.

Time Step Size

16

See Section 14.3.1 above for the choice of time step size for explicit algorithms on general curvilinear meshes. The time step sizes used on the mesh shown above were for Case (1) $\Delta t = cfl \cdot \Delta t_{max} \simeq 0.62 \times 10^{-4}$ sec. and for Case (2) $\Delta t = cfl \cdot \Delta t_{max} \simeq 0.56 \times 10^{-4}$ sec. per time step during the calculation, where the factor $cfl = 0.9$.

Solutions
Run your program until convergence, about 400 time steps.

Case (1) $M_\infty = 0.735$
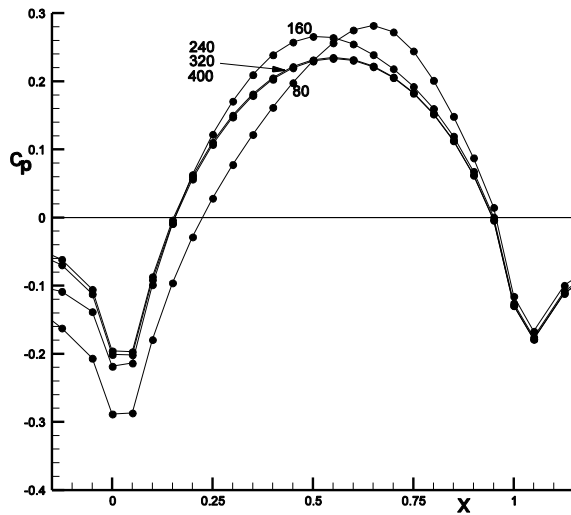
Figure 14.15a c_p vs. x, Mod-Steger-Warming I
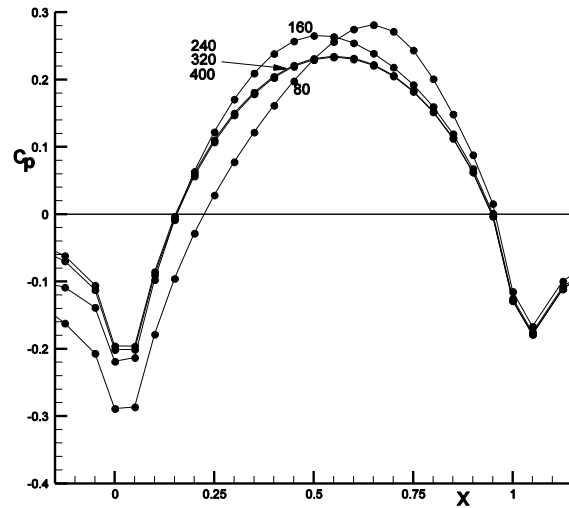
Figure 14.15b c_p vs. x, Roe Method
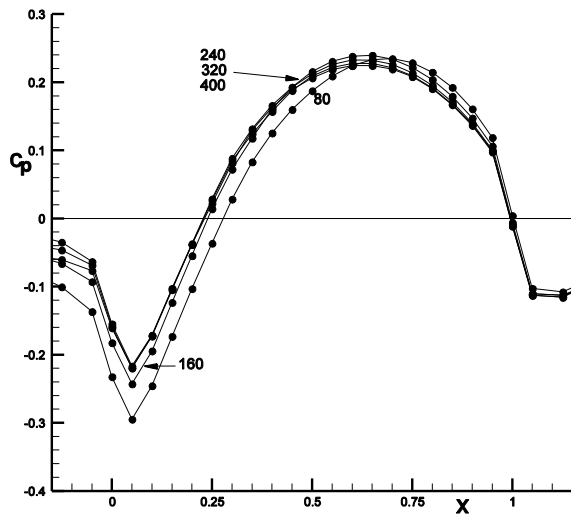
Figure 14.15c c_p vs. x, Steger-Warming
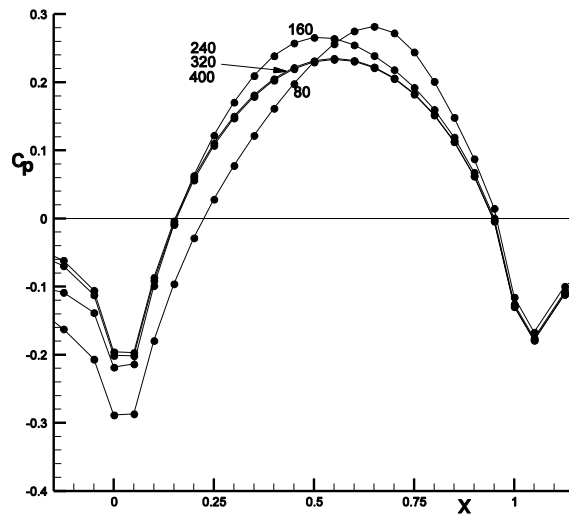
Figure 14.15d c_p vs. x, Mod-Steger-Warming II

Case (2) $M_\infty = 0.908$
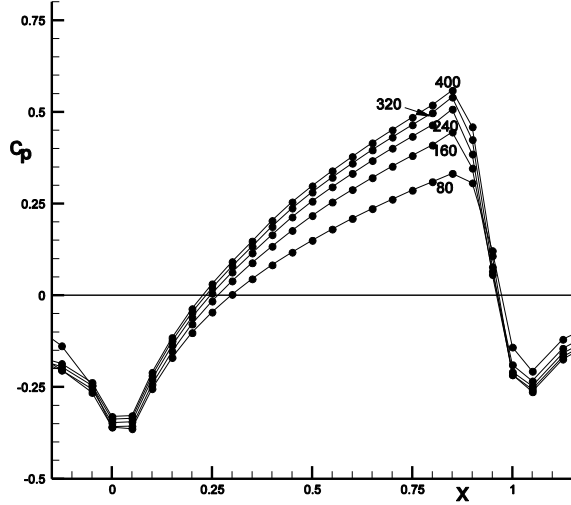
Figure 14.16a c_p vs. x, Mod-Steger-Warming I
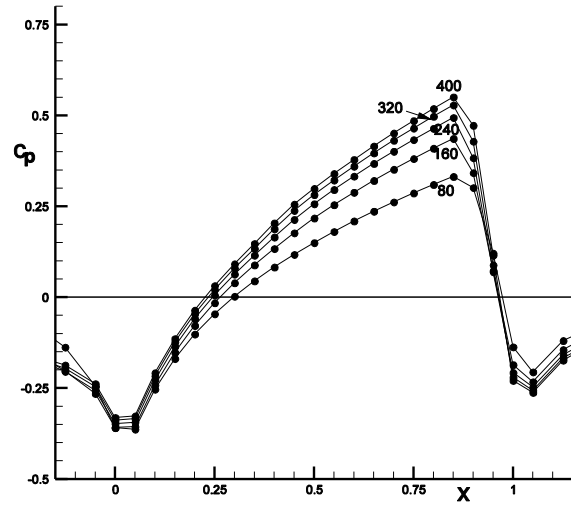
Figure 14.16b c_p vs. x, Roe Method
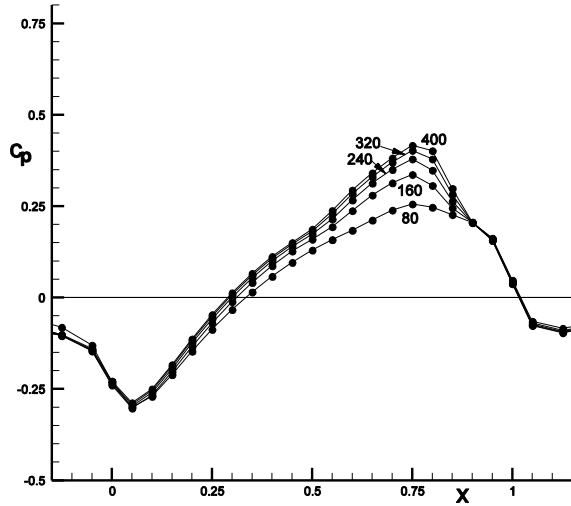
Figure 14.16c c_p vs. x, Steger-Warming
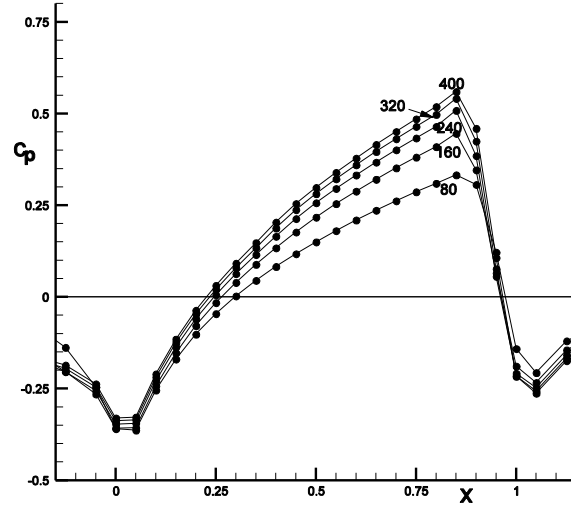
Figure 14.16d c_p vs. x, Mod-Steger-Warming II

The results above show that the solutions using the Modified-Steger-Warming methods, versions I and II, and the Roe method agree closely with one another, but the pure Steger-Warming method is too dissipative.

 The mesh used for the solutions shown above is too course near the leading and trailing edges. The results shown below cluster points in these regions using the same stretching function discussed above. A mesh 101x101 points was used with 40 along the airfoil surface. Because the fineness of the mesh will severely restrict the allowed time step size for an explicit method, the *implicit* version of the Modified-Steger-Warming Method II was used with *cfl* numbers approaching 50. Both first order accurate and second order accurate solutions are shown.

Fine Mesh Solutions, 1st order, Implicit Modified-Steger-Warming, Version II

18

Figure 14.17 Fine mesh near airfoil.

Case(1) $M_\infty = 0.735$

Figure 14.18 c_p vs. x, 1st order

Figure 14.19 Mach contours, 1st order

Case(2) $M_\infty = 0.908$

Figure 14.20 c_p vs. x, 1st order

Figure 14.21 Mach contours, 1st order

19

Case(1)
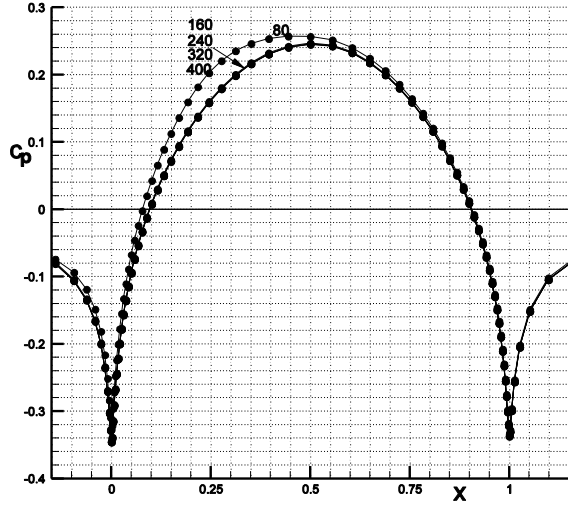
Figure 14.22 c_p vs. x, 2nd order
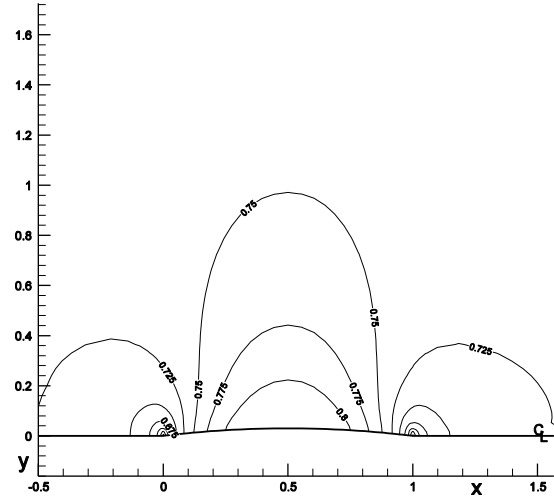
Figure 14.23 Mach contours, 2nd order

Case(2)
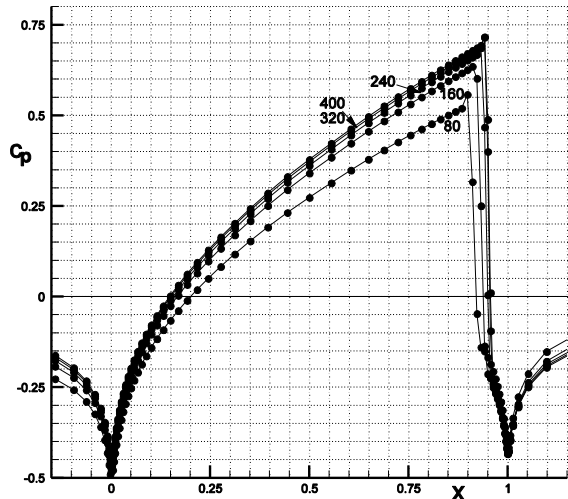
Figure 14.24 c_p vs. x, 2nd order
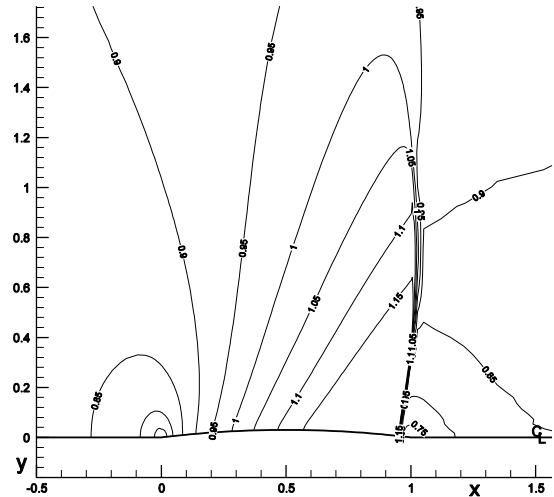
Figure 14.25 Mach contours, 2nd order

The final solution taken from Figure 14.24 above has been added to Figure 8.8 of Chapter 8 for comparison with the solutions to the Full Potential and Transonic Small Disturbance equations, as shown in the figure below. Strangely, here again (see Figure 1.6 of Chapter 1) the Transonic Small Disturbance equation solution agrees better with the inviscid Euler solution for shock strength and location than the more exact Full Potential equation. The horizontal dashed line indicates the value of c_p^*, the value of c_p at sonic points.
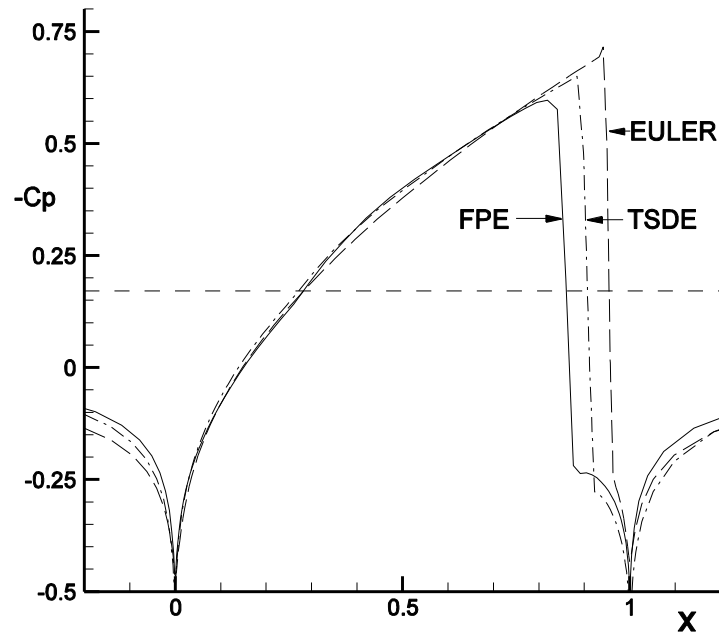
Figure 14.26 Comparison of solutions to the Euler, Full Potential
and Transonic Small Disturbance equations for Case (2)
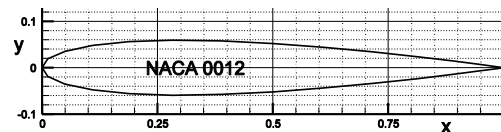
Figure 14.27 NACA0012 airfoil

14.3.3 Flow Past an NACA0012 Airfoil
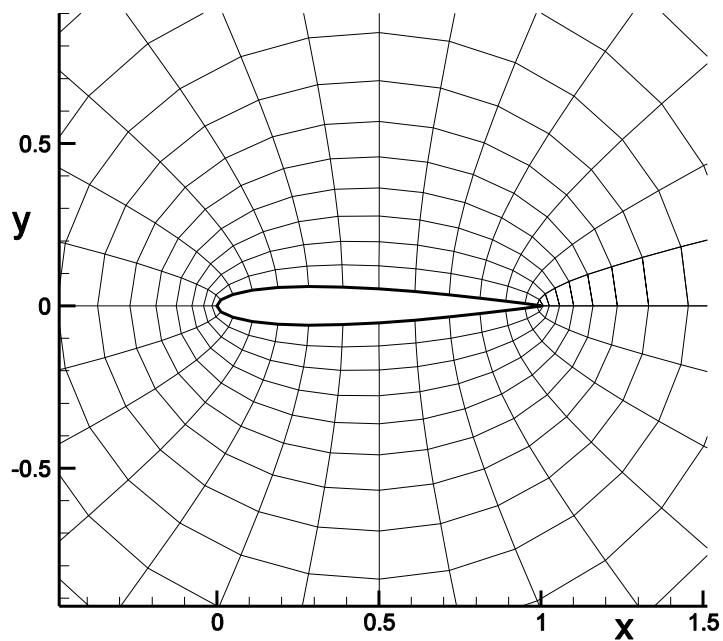
Figure 4.28 Mesh about an NACA0012 airfoil**.**

Exercise(3): Solve for $M_\infty = 0.75$ flow past an NACA0012 airfoil of chord length $c = 1$ for Case (1) at 0° angle of attack and Case (2) at 1° angle of attack, on a 30×30 mesh, with 28 non-equally-spaced points wrapped about the airfoil and 30 stretched from the body surface to the far field boundary at 50 chord lengths away. The coordinates for the airfoil shape are given in Section 8.4.4 (complete descriptions for NACA airfoils can be found now on the Internet)

Solution Approach: The airfoil chord length $c = 1m$. and the flow has a total pressure and temperature near atmospheric, $p_t = 1.0 \times 10^5 N/m^2$ and $T_t = 300^o K$. The O-type mesh near and about the airfoil is shown in the figure above. The grid was constructed first for an ellipse with the same thickness to chord ratio as the airfoil and then modified using the surface geometry data of the NACA0012 airfoil to relocate the points along the airfoil surface. A compound stretching described below was used to fill out the mesh, from the airfoil surface to the far field boundary.

A Compound Stretching Function
The first mesh point located at the airfoil surface is denoted by $y_2 = 0$, the spacing $\Delta y_{min} = y_3 - y_2$ and $JLFM = 20$. The coordinate y is used here to represent the radial direction, from airfoil surface to the outer boundary $50c$ away.

$$y_j = y_{fm} \frac{e^{\kappa \frac{j-2}{JLFM-2}} - 1}{e^\kappa - 1}$$

We define the first equation, for which we need to find values for κ and y_{fm}

$$f_1(\kappa, y_{fm}) = \Delta y_{min} - (y_3 - y_2) = \Delta y_{min} - y_{fm} \frac{e^{\kappa \frac{1}{JLFM-2}} - 1}{e^\kappa - 1} = 0$$

The coarse mesh spacing is defined by, with $JL = 30$ and $H = 50c$,

$$\Delta y_{cm} = \frac{H - y_{fm}}{JL - JLFM}$$

We define a second function, such that Δy_{cm} equals the spacing of the fine mesh if continued one more mesh point into the coarse mesh.

$$f_2(\kappa, y_{fm}) = \frac{H - y_{fm}}{JL - JLFM} - \left(y_{fm} \frac{e^{\kappa \frac{JLFM-1}{JLFM-2}} - 1}{e^\kappa - 1} - y_{fm} \right) = 0$$

We solve these two equations simultaneously using Newton's iteration method for vector functions.

$$A_k(X_{k+1} - X_k) = -F(X_k)$$

where the Jacobian matrix $A = \dfrac{\partial F}{\partial X}$ and the vectors $X = \begin{bmatrix} \kappa \\ y_{fm} \end{bmatrix}$ and $F = \begin{bmatrix} f_1(\kappa, y_{fm}) \\ f_2(\kappa, y_{fm}) \end{bmatrix}$

Notice the similarity to, or extension of, Newton's procedure for the scalar equation case. Start with $X_1 = \begin{bmatrix} 1 \\ H/10 \end{bmatrix}$ and use 10 iterations, usually more than sufficient to find values for κ and y_{fm} that satisfy the two equations $f_1(\kappa, y_{fm}) = 0$ and $f_2(\kappa, y_{fm}) = 0$.

Boundary Conditions:
The figures below show the total mesh and a schematic of the flow field.
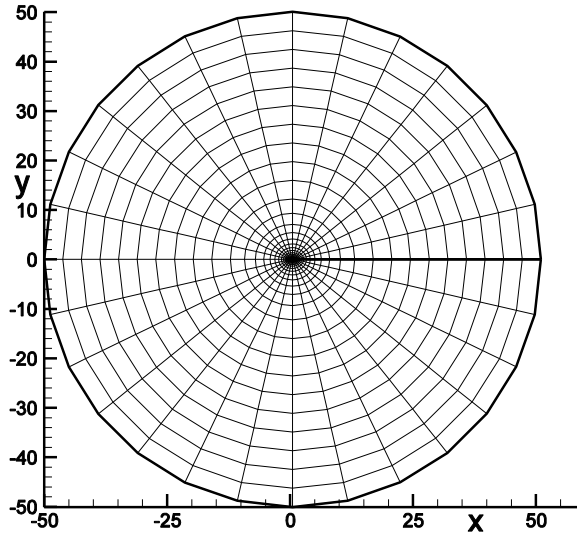
Figure 14.29 Total mesh   **Figure 14.30** Flow volume about airfoil
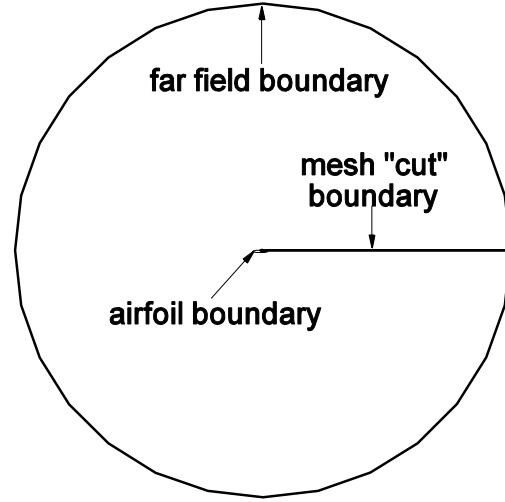
The airfoil boundary, not visible in the figures above because of their large scale, is treated in the same way as the flow about the circular arc airfoil. Conditions at the far field boundary are held fixed to their initial values. The mesh is cut along a line starting at the trailing edge of the airfoil and extending to the right far field boundary. Starting at the cut line and then moving along a mesh curve circumnavigating about the airfoil in a clockwise direction θ will increase from 0 to 2π, returning to the cut line again. The boundary conditions at the or across the cut line are therefore periodic.

For the *finite difference* approach the index $i = 1$ at the cut line at the start and $i = 29$ at the cut line at the end of the round trip. Therefore, the boundary conditions are given by $U_{1,j}^n = U_{29,j}^n$ and $U_{30,j}^n = U_{2,j}^n$. Tthese mesh point values are located at the mesh line intersections.

For the *finite volume* approach the index $i = 1+1/2$ at the start of the cut line and $i = 29+1/2$ at the end of the cut line after completing the round trip. Therefore, the boundary condition is given

by $U_{1,j}^n = U_{29,j}^n$ and $U_{30,j}^n = U_{2,j}^n$. These mesh point values are located at the centers of the volume elements formed by the mesh lines (see Figure 8.21 in Chapter 8).

Solutions

Run your program until convergence, about 800 time steps. The solutions shown below were obtained using Modified-Steger-Warming II algorithm.
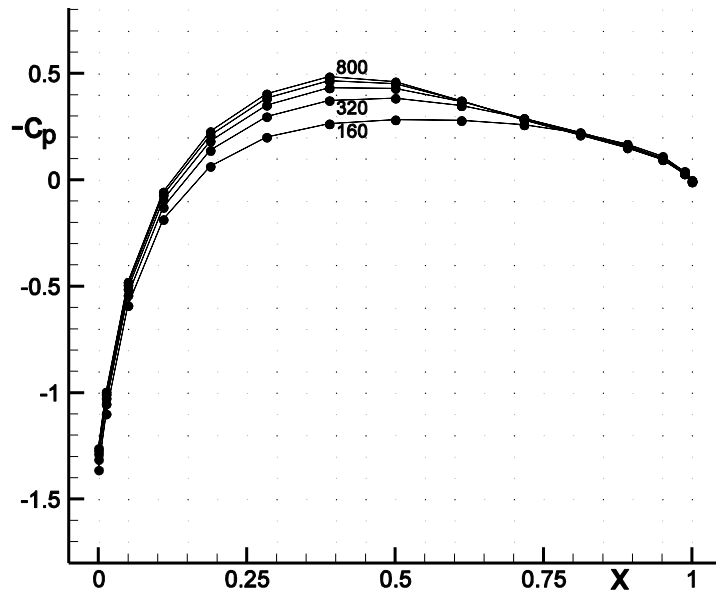

Figure 14.31 Convergence of c_p vs. x for flow Case(1).

Solutions for Case (1) and (2) after 800 time steps are shown below. Both the upper and lower surface c_p distributions are shown in each figure.
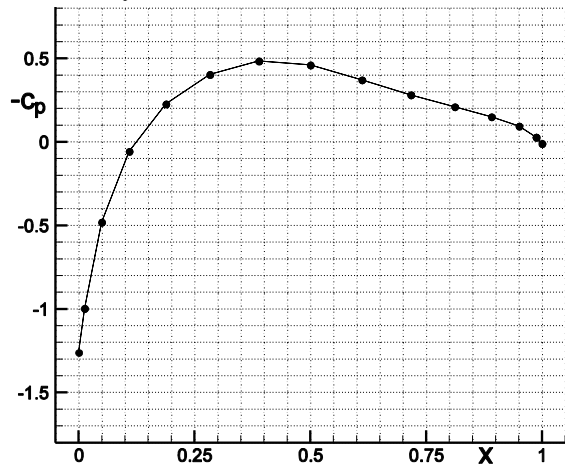
Figure 14.32 c_p vs. x for Case (1), $\alpha = 0^o$
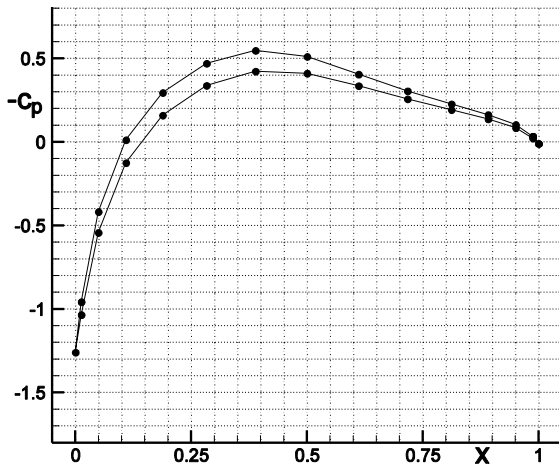
Figure 14.33 c_p vs. x for Case (2), $\alpha = 1^o$

The two cases shown above were not run long enough to reach convergence. They were rerun using the implicit methods described in Chapter 11, modified for the circular grid described in Section

24

8.3.3.1 for a periodic matrix solution, using matrices with 4x4 block element matrices instead of scalar elements. Three different grids were used, course 30x30, medium 60x60 and fine 120x120, as shown below near the airfoil surface. The solutions were run for about 100 time steps, during which the flow moved about 17 chord lengths.
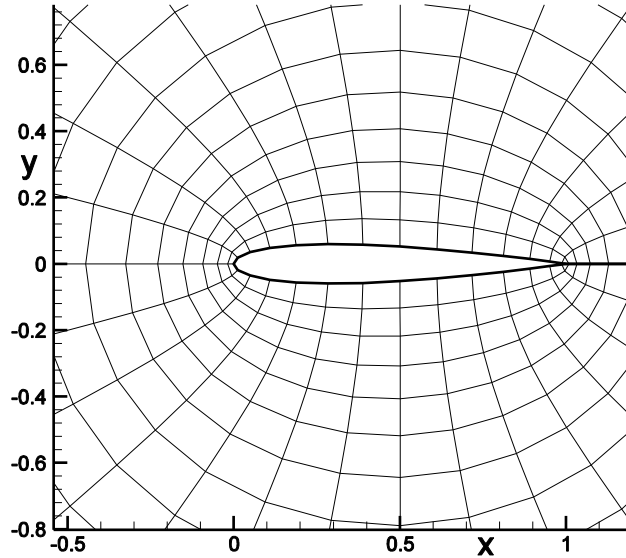
Figure 14.34 NACA coarse grid
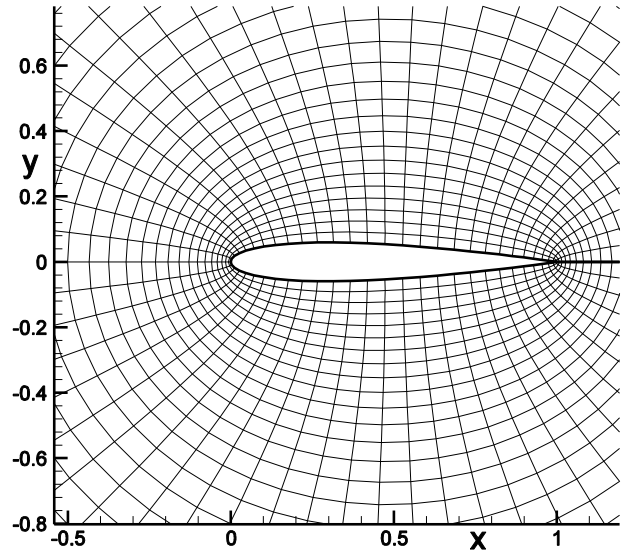
Figure 14.35 NACA medium grid
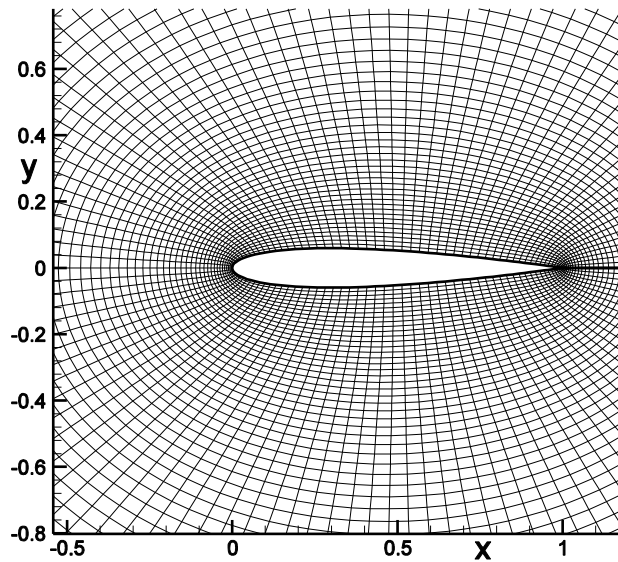
Figure 14.35 NACA fine grid

The solutions on these three grids for case (1) with $M_\infty = 0.75$ flow past a NACA 0012 airfoil at zero angle of attack are shown below. Note the possible development of a shock wave as grid refinement proceeds in the c_p distribution plots. Both the upper and lower surface c_p distributions are shown to lie on top of one another. Compare with that of Figure 8.19 for the solution of the full potential equation. The dashed line in the figures represents c_p^*, the value of the pressure

coefficient c_p at sonic points, $V = a = \sqrt{\gamma \dfrac{p}{\rho}}$, divides supersonic and subsonic values, and indicates possible shock waves locations.
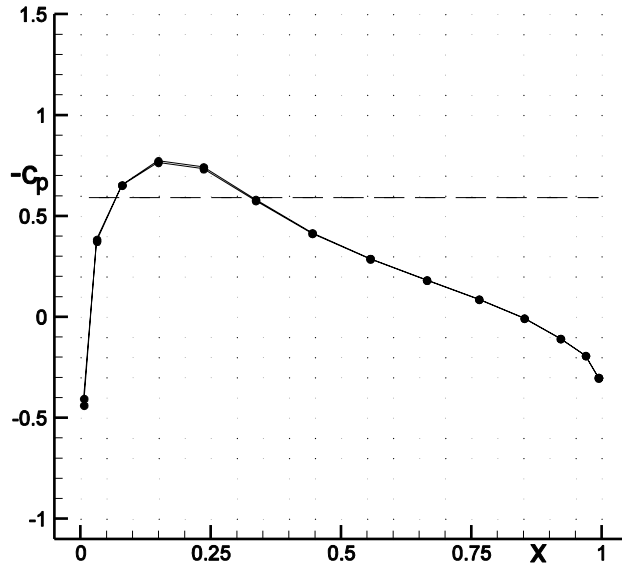
Figure 14.36 Coarse grid c_p distribution
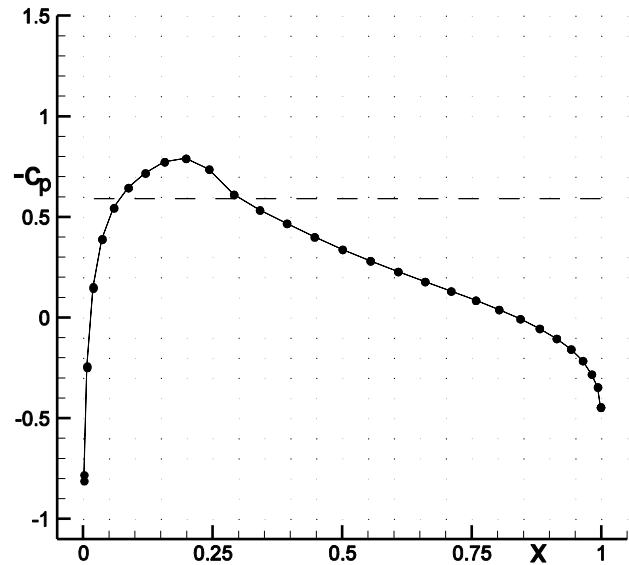
Figure 14.37 Medium grid c_p distribution
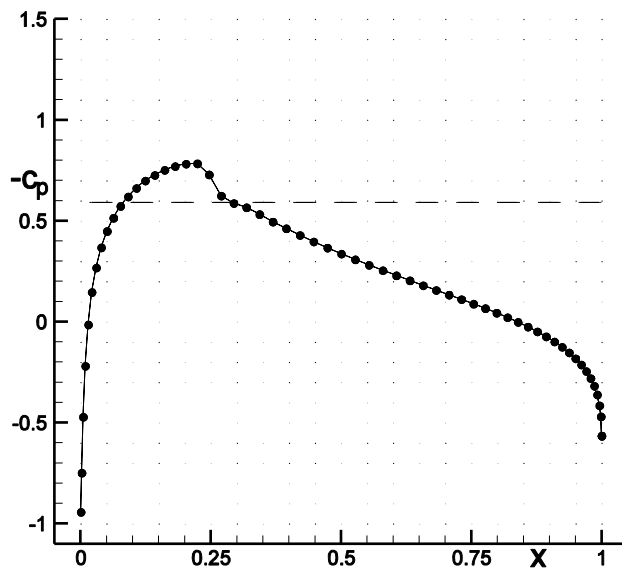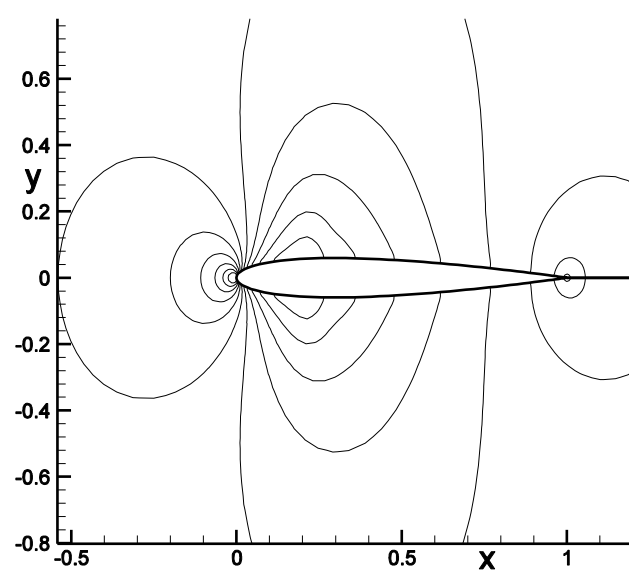

Figure 14.36 Fine grid c_p distribution

Figure 14.37 Fine flow field

The solutions on these three grids for case (2) with $M_\infty = 0.75$ flow past a NACA 0012 airfoil at 1 degree angle of attack are shown below. Note here the clear development of a shock wave as grid refinement proceeds. Compare with that of Figure 8.20 and Figures 8.22-25 for the solutions of the full potential equation. Note that, unlike the full potential equation, no special treatment is required to satisfy the Kutta condition at the airfoil trailing edge. The full potential equation represents only the physics of the continuity equation, "the conservation of mass". The Euler equations also

represent the conservation of momentum and energy. The momentum equations have built into them the consequences of centrifugal force when turning the flow about a small radius of curvature, principally a reduction of pressure about a convex surface (see Section 12.2.1.1). A sharp corner will cause a severe adverse pressure gradient for any flow about the corner, forcing the streamlines to satisfy the Kutta condition at the corner.
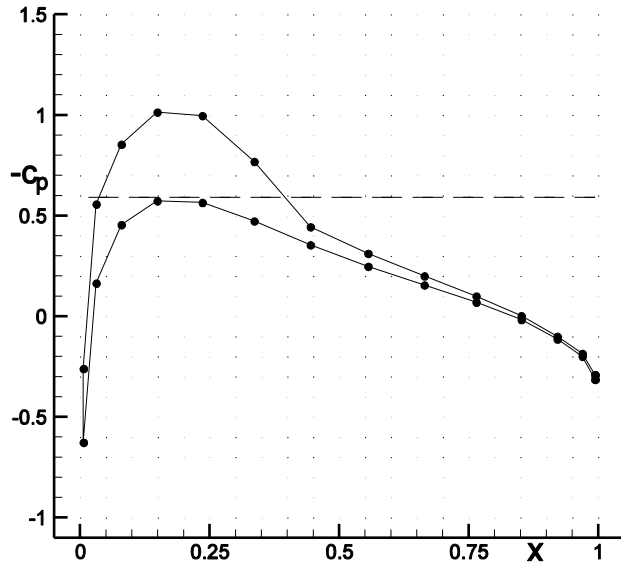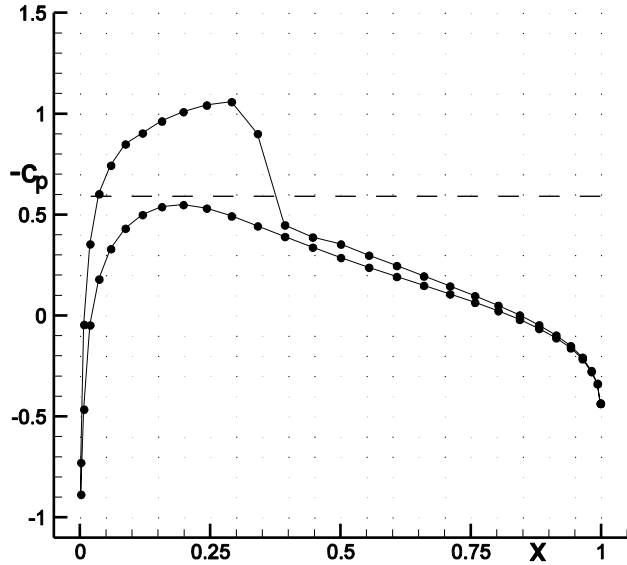

Figure 14.38 Coarse grid c_p distribution

Figure 14.39 Medium grid c_p distribution
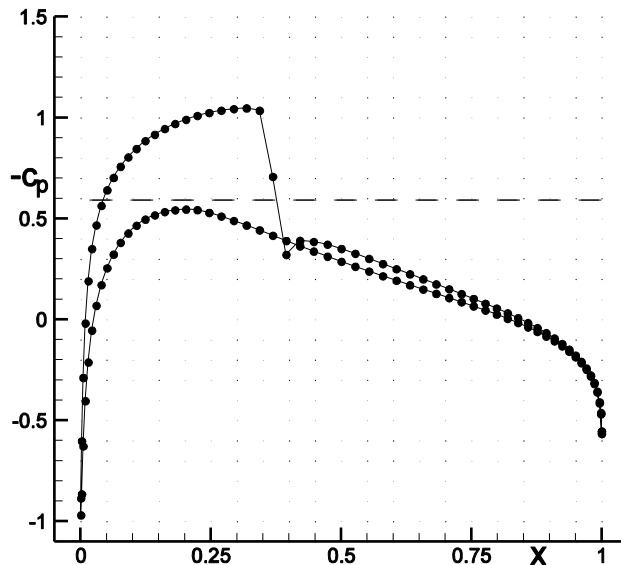
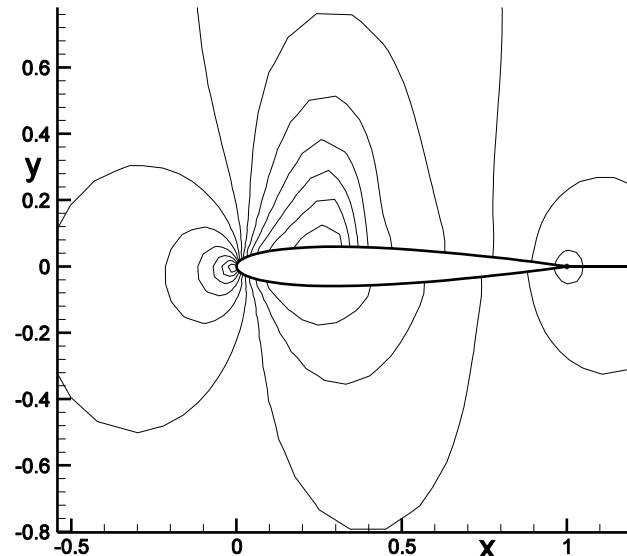**Figure 14.40** Fine grid c_p distribution

Figure 14.41 Fine flow field

14.3.4 Flow Past an Ellipse

The flow problem of the exercise in Section 8.4.3, $M_\infty = 0.2$ flow past a $6-1$ ellipse at 5° angle of attack, was calculated using the Euler equations, on three different grids extending 50 chords away

from the ellipse. The grids are shown near the ellipse in the figures below. The grids are 30x30, 60x60 and 120x120.
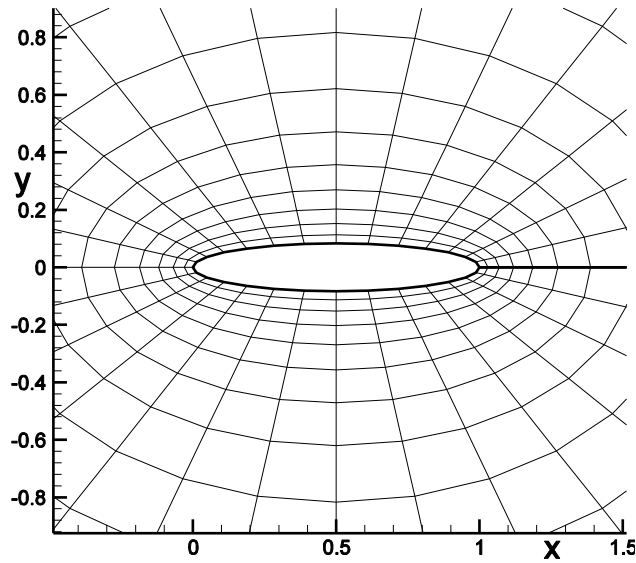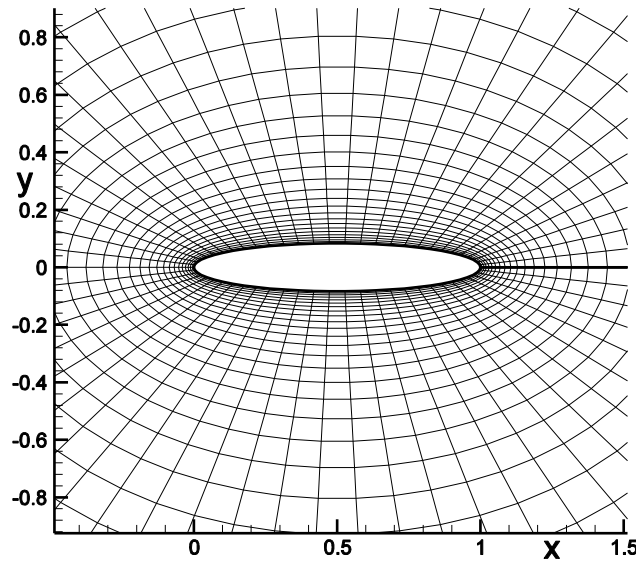

Figure 14.42 Coarse grid about ellipse

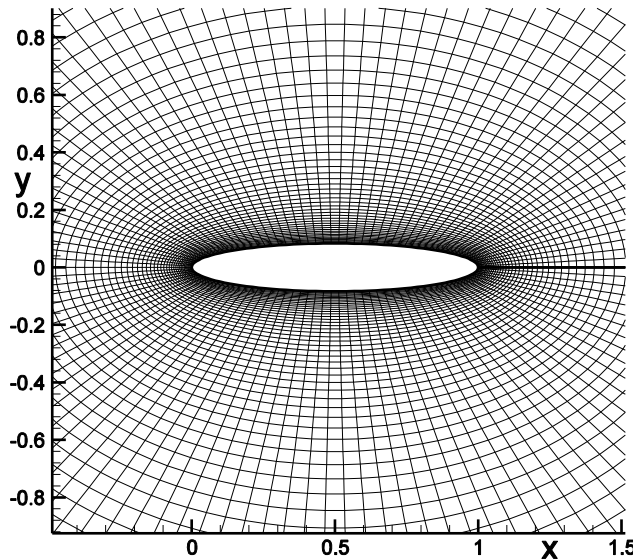**Figure 14.43** Medium grid about ellipse

Figure 14.44 Fine grid about ellipse

The c_p distributions for the three different grids are shown below. They were obtained using the Modified-Steger-Warming II algorithm. Compare these results with those shown in Figure 8.16. The c_p distribution of Figure 8.16 appears perfectly symmetric with no apparent drag or lift. Those below are less perfect with the coarse grid solution appearing, understandably, the worst of the three. This illustrates the difficulty of solving the Euler equations at low Mach numbers. The solutions shown below were run for about 200 time steps, during which the flow moved approximately 5 body lengths.
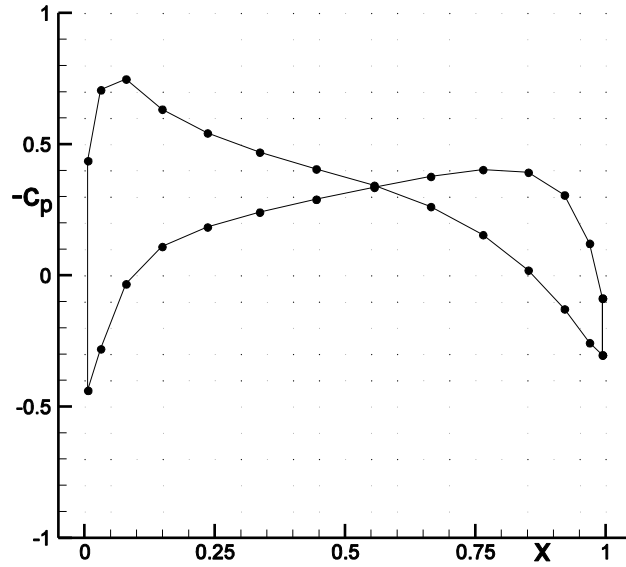
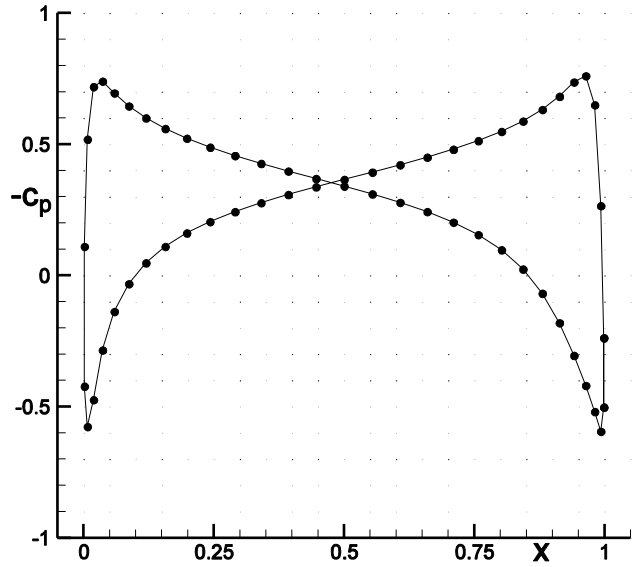**Figure 14.45** Coarse grid c_p distribution

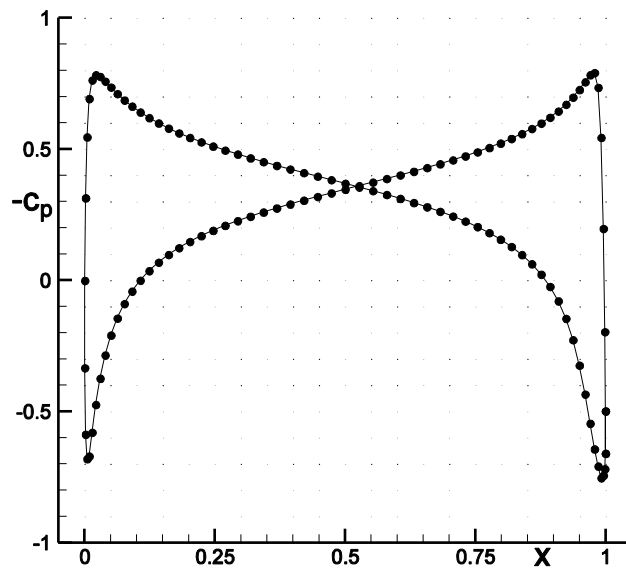**Figure 14.46** Medium grid c_p distribution

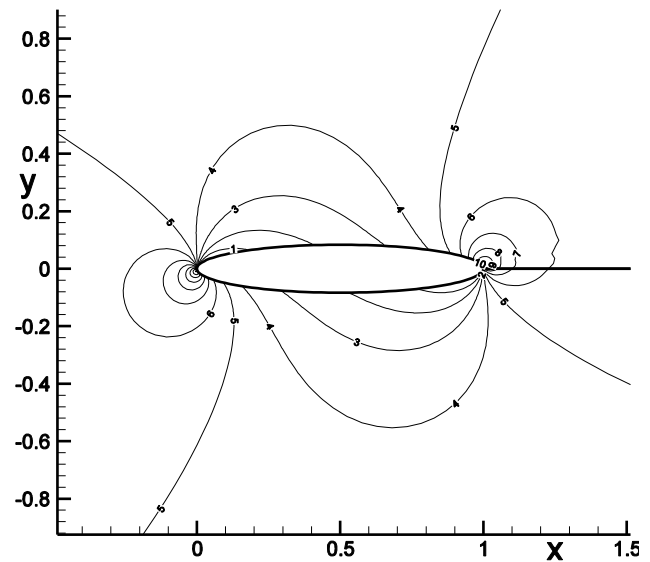**Figure 14.47** Fine grid c_p distribution

Figure 14.48 Fine flow field

14.4 The Euler Equations in Axisymmetric Arbitrary Coordinates

The two dimensional Euler equations in arbitrary curvilinear coordinates can be easily modified for solving axisymmetric flow problems. The two dimensional equations given previously are plane symmetric. They can be thought of as governing the flow between two planes normal to the z-coordinate, spaced a unit distance apart, and for which all derivatives with respect to z vanish. An axisymmetric flow can be thought of as the flow between two planes passing through a common axis, the x axis in our case, with angle $\Delta\theta$ between them, for which all derivatives with respect to θ vanish.
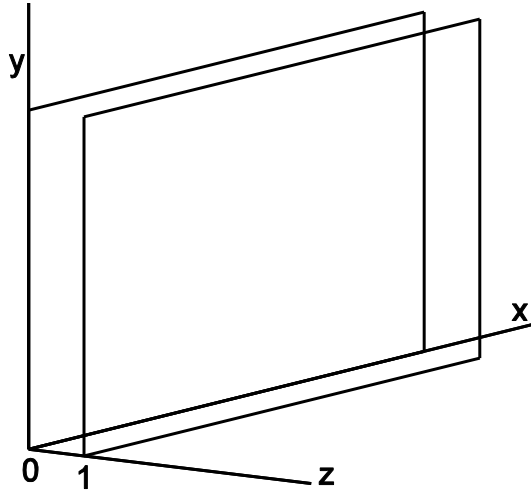
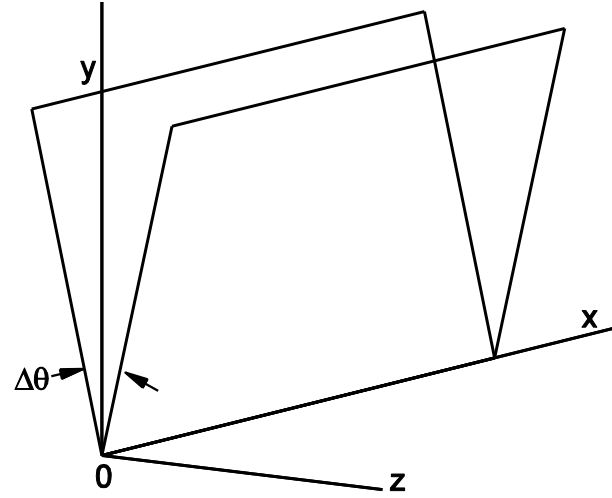**Figure 14.49** 2-D plane symmetric   **Figure 14.50** 2-D axisymmetric
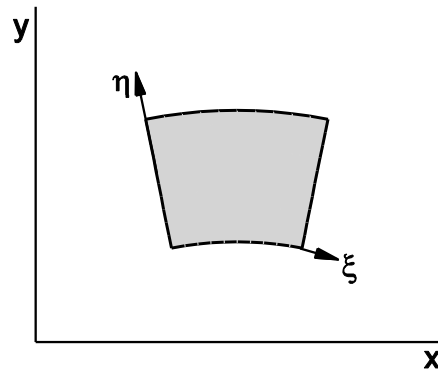

Figure 14.51 Arbitrary volume in two dimensional space

Consider the two dimensional finite control volume shown in Figure 14.51. The base area is smaller than that at the top. In a constant pressure field the top would experience a downward force greater than the upward force at the base. This net force acting down would be counter balanced by components of the forces acting on the left and right side surfaces to produce a zero sum force acting on the body. Again, the two dimensional finite volume of Figure 14.51 can be viewed as an actual three dimensional volume by assuming unit depth normal to the plane of the figure, as shown in Figure 14.52. The two dimensional finite control volume of Figure 14.51 can be rotated about the x-axis through angle $\Delta\theta$ for axisymmetric flow, as shown below in Figure 14.53.
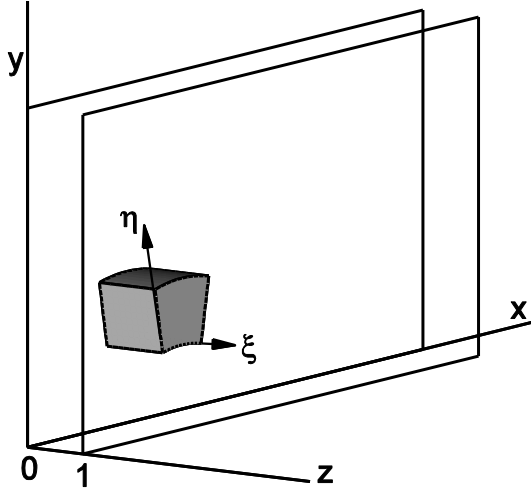
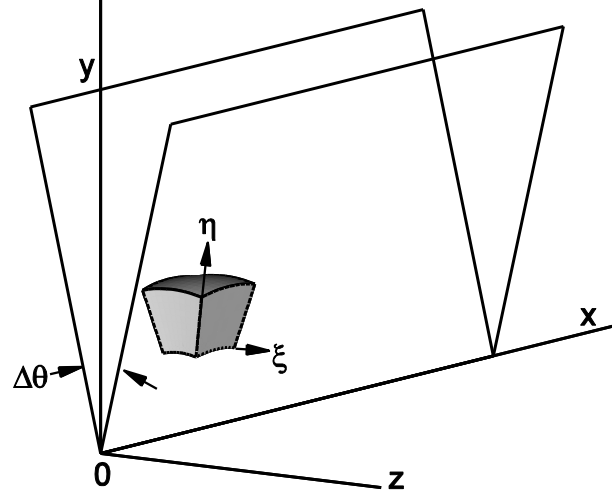**Figure 14.52** Volume in 2-D plane symmetry

Figure 14.53 Arbitrary axisymmetric volume

The flow passing through the axisymmetric control volume is still strictly two dimensional. If we again consider a uniform pressure field, the force acting down at the top surface of the axisymmetric volume is even further out of balance with that acting up at the lower surface because of the increase in surface area with the radial distance away from the axis of symmetry. The vertical components of force acting on the left and right sides can no longer counter balance the difference. Although all derivatives in the θ-direction vanish and there is no net flow through the two side faces on planes of constant θ, the fluid stresses acting on these faces are needed to balance those in the radial y direction. Just the following two effects, need to be included to convert a plane two dimensional flow program into an axially symmetric one.

1) *the changes in surface areas and volumes caused by changes with radial location*, and
2) *the additional stresses that act at volume faces orthogonal to the θ-direction*,

These two effects are discussed in turn below.

14.4.1 Surface Area and Volume Changes
Plane two dimensional arbitrary coordinates
The flux vectors in an arbitrary two-dimensional curvilinear plane-symmetric coordinate system are

$$F'^{2D} = \left(\frac{\partial y}{\partial n} \Delta\eta F - \frac{\partial x}{\partial n} \Delta\eta G \right) \Delta z \quad and \quad G'^{2D} = \left(-\frac{\partial y}{\partial \xi} \Delta\xi F + \frac{\partial x}{\partial \xi} \Delta\xi G \right) \Delta z$$

where $\Delta\xi$, $\Delta\eta$ and Δz are each equal to one. The flux vector F'^{2D} acts on the surface element at $\xi = i+1/2$ and G'^{2D} acts on the surface element at $\eta = j+1/2$. These two dimensional surface elements can be defined as

$$\vec{S}_\xi^{2D} = \left(\frac{\partial y}{\partial \eta} \Delta\eta\, \vec{i}_x - \frac{\partial x}{\partial \eta} \Delta\eta\, \vec{i}_y \right) \Delta z \quad and \quad \vec{S}_\eta^{2D} = \left(-\frac{\partial y}{\partial \xi} \Delta\xi\, \vec{i}_x + \frac{\partial x}{\partial \xi} \Delta\xi\, \vec{i}_y \right) \Delta z$$

and the volume element, can be expressed as $\quad V_{i,j}^{2D} = \left(\dfrac{\partial x}{\partial \xi} \dfrac{\partial y}{\partial \eta} - \dfrac{\partial x}{\partial \eta} \dfrac{\partial y}{\partial \xi} \right)_{i,j} \Delta \xi \, \Delta \eta \, \Delta z$

where the metric partial derivative terms are defined in Section 7.8, for both the finite difference approach and the finite volume approach. The plane two dimensional fluxes at surface elements $\vec{S}_\xi^{2D}$ and $\vec{S}_\eta^{2D}$ can also be defined by vector "dot" products.

$$F'^{2D} = \left(F \, \vec{i}_x + G \, \vec{i}_y \right) \cdot \vec{S}_\xi^{2D} \quad \text{and} \quad G'^{2D} = \left(F \, \vec{i}_x + G \, \vec{i}_y \right) \cdot \vec{S}_\eta^{2D}$$

__Axisymmetric two dimensional arbitrary coordinates__
The corresponding axisymmetric surface elements are defined below, where $\bar{y}$ below acts as the radial coordinate.

$$\vec{S}_\xi^{axi} = \left(\frac{\partial y}{\partial \eta} \Delta \eta \, \vec{i}_x - \frac{\partial x}{\partial \eta} \Delta \eta \, \vec{i}_y \right) \bar{y}_\xi \Delta \theta \quad \text{and} \quad \vec{S}_\eta^{axi} = \left(-\frac{\partial y}{\partial \xi} \Delta \xi \, \vec{i}_x + \frac{\partial x}{\partial \xi} \Delta \xi \, \vec{i}_y \right) \bar{y}_\eta \Delta \theta$$

and the axisymmetric volume element by $\quad V_{i,j}^{axi} = \left(\dfrac{\partial x}{\partial \xi} \dfrac{\partial y}{\partial \eta} - \dfrac{\partial x}{\partial \eta} \dfrac{\partial y}{\partial \xi} \right)_{i,j} \Delta \xi \, \Delta \eta \, \bar{y}_{i,j} \Delta \theta$

The difference between the 2D and axisymmetric surface and volume element definitions is just the replacement of Δz with $\bar{y} \Delta \theta$, for small $\Delta \theta \simeq \pi / 180$. Note: from a purely geometric point of the view $\Delta \theta$ factor should be replaced by $2 \sin(\Delta \theta / 2)$. However, the $\Delta \theta$ factor in the surface element definitions will cancel that in the volume definitions, i.e.

$$U_{i,j}^{n+1} = U_{i,j}^n - \frac{\Delta t}{V_{i,j}^{axi}} \left(\frac{\vec{F}_{i+1/2,j}^n \cdot \vec{S}_{i+1/2}^{axi} - \vec{F}_{i-1/2,j}^n \cdot \vec{S}_{i-1/2}^{axi}}{\Delta \xi} + \dots \right),$$

and can therefore be completely arbitrary, even $\Delta \theta = 1$. The $\bar{y}$ quantities are defined below as the average values of y, using the corner points defining the surface elements or the volume center. For example, using Figure 14.51 for the arbitrary mesh volume, with mesh point locations as defined in Figure 14.7,

$$\bar{y}_{\xi=i+1/2} = \frac{1}{2} \left(y_{i+1,j+1} + y_{i+1,j} \right) \quad \text{and} \quad \bar{y}_{\eta=j+1/2} = \frac{1}{2} \left(y_{i+1,j+1} + y_{i,j+1} \right)$$

and for the volume element, $\bar{y}_{i,j}$ is the average of the four corner points.

$$\bar{y}_{i,j} = \frac{1}{4} \left(y_{i,j} + y_{i+1,j} + y_{i,j+1} + y_{i+1,j+1} \right)$$

The axisymmetric flux vectors at surface elements $\vec{S}_\xi^{axi}$ and $\vec{S}_\eta^{axi}$ are then

$$F'^{axi} = \left(F\,\vec{i}_x + G\,\vec{i}_y \right) \cdot \vec{S}_{\xi}^{axi} \qquad \text{and} \qquad G'^{axi} = \left(F\,\vec{i}_x + G\,\vec{i}_y \right) \cdot \vec{S}_{\eta}^{axi}$$

or

$$F'^{axi} = \left(\frac{\partial y}{\partial n} F - \frac{\partial x}{\partial n} G \right) \overline{y}_{\xi} \Delta\theta \quad and \quad G'^{axi} = \left(-\frac{\partial y}{\partial \xi} F + \frac{\partial x}{\partial \xi} G \right) \overline{y}_{\eta} \Delta\theta$$

Similarly, the rotated axisymmetric Jacobians are

$$A'^{axi} = \frac{\partial F'^{axi}}{\partial U} = \left(\frac{\partial y}{\partial n} A - \frac{\partial x}{\partial n} B \right) \overline{y}_{\xi} \Delta\theta \quad and \quad B'^{axi} = \frac{\partial G'^{axi}}{\partial U} = \left(-\frac{\partial y}{\partial \xi} A + \frac{\partial x}{\partial \xi} B \right) \overline{y}_{\eta} \Delta\theta$$

Note that in each case above, the modification of a 2D quantity to produce an axisymmetric one involved only the multiplication by an appropriate $\overline{y}$ that accounted for the geometrical difference between plane and axial symmetry. Besides this geometric modification, the governing equations also need to be modified to include the effects of the surface stresses acting on the surfaces orthogonal to the θ direction, given in the next section.

14.4.2 Additional Surface Stresses

Because of the expansion of surface area with radial distance y, additional stresses have to be included to balance the y momentum equation in much the same manner that the inhomogeneous Q vector term was added to the right hand side of the Quasi 1-D Euler equations given in Chapter 7, Section 7.5.1. These stresses act on the two surface faces at constant θ, shown in Figure 14.53 for an arbitrary axisymmetric volume. The equation for axisymmetric flow becomes

$$\frac{\partial U}{\partial t} + \frac{1}{V^{axi}} \frac{\partial F'^{axi}}{\partial \xi} + \frac{1}{V^{axi}} \frac{\partial G'^{axi}}{\partial \eta} = Q^{axi} = \frac{\Delta S^{axi}}{V^{axi}} \begin{bmatrix} 0 \\ 0 \\ p \\ 0 \end{bmatrix}$$

where ΔS represents the sum of the y components of the surface areas of the two surface elements at constant θ. This area is also the sum of the projected areas of these surfaces on the $x-z$ plane. It is also equivalent to the difference in the surface areas projected by the other four surface elements.

$$\Delta S_{i,j}^{axi} = \left(\vec{S}_{\xi=i+1/2}^{axi} + \vec{S}_{\eta=j+1/2}^{axi} - \vec{S}_{\xi=i-1/2}^{axi} - \vec{S}_{\eta=j-1/2}^{axi} \right) \cdot \vec{i}_y$$

$$= \left(-(x_{i+1,j+1} - x_{i+1,j}) \overline{y}_{\xi=i+1/2} + (x_{i+1,j+1} - x_{i,j+1}) \overline{y}_{\eta=j+1/2} + (x_{i,j+1} - x_{i,j}) \overline{y}_{\xi=i-1/2} - (x_{i+1,j} - x_{i,j}) \overline{y}_{\eta=j-1/2} \right) \Delta\theta$$

Finally, for implicit methods the Jacobian of Q^{axi} with respect to U will need to calculated, as follows.

$$\frac{\partial Q^{axi}}{\partial U} = \frac{\Delta S^{axi}}{V^{axi}} \begin{bmatrix} 0 & 0 & 0 & 0 \\ 0 & 0 & 0 & 0 \\ \alpha\beta & -u\beta & -v\beta & \beta \\ 0 & 0 & 0 & 0 \end{bmatrix}, \qquad \text{where } \alpha = \frac{u^2 + v^2}{2} \text{ and } \beta = \gamma - 1$$

Note: If the mesh is Cartesian in the $x - y$ plane,

$$\vec{S}_\xi^{axi} = \Delta y \, \bar{y}_\xi \Delta\theta , \qquad \vec{S}_\eta^{axi} = \Delta x \, \bar{y}_\eta \Delta\theta , \qquad V_{i,j}^{axi} = \Delta x \, \Delta y \, \bar{y}_{i,j} \Delta\theta \qquad \Delta S_{i,j}^{axi} = \Delta x \Delta y \Delta\theta$$

and the differential equation for axisymmetric flow becomes, with the $\bar{y}$'s replaced by y,

$$\frac{\partial U}{\partial t} + \frac{\partial F}{\partial x} + \frac{1}{y}\frac{\partial G \, y}{\partial y} = Q^{axi} = \frac{1}{y}\begin{bmatrix} 0 \\ 0 \\ p \\ 0 \end{bmatrix}$$

The above equation is the usual expression for the Euler equations in cylindrical coordinates, where the radial coordinate r has been replaced by y.
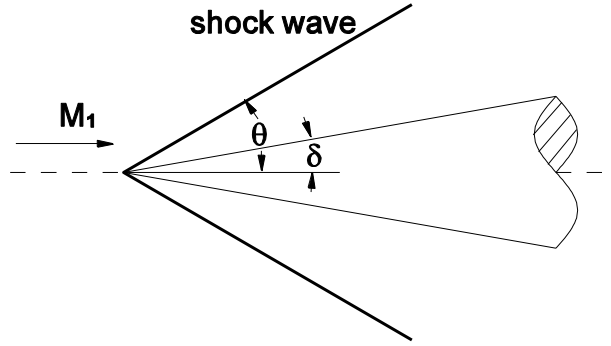
14.4.3 Conical Flow

Figure 14.54 Flow Past a Cone

The flow past a cone differs from that for a wedge because of the three dimensional relief effect, which weakens the shock wave and causes the streamlines to move closer to the cone surface with distance, as shown in Figure 14.55. Thus, the shock wave about the cone is swept back further for the same cone half angle δ, as the wedge angle δ, and for the same free stream Mach number. As for supersonic flow past a wedge, there is no reference length for flow past an infinite slender cone. The only relevant geometric feature is the angle measured from the axis of symmetry. The flow is therefore constant along each ray through the cone apex, as shown in Figure 14.56. Thus, the flow along the body surface is constant. Taylor and Maccoll have found conical flow solutions as early as 1933. For example, for Mach two flow past a cone with $\delta = 10^o$, the oblique shock wave angle

is $\theta \simeq 31.2^o$ and the pressure ratio along the cone surface is $\dfrac{p_2}{p_1} \simeq 1.29$. For a $\delta = 20^o$ half angle

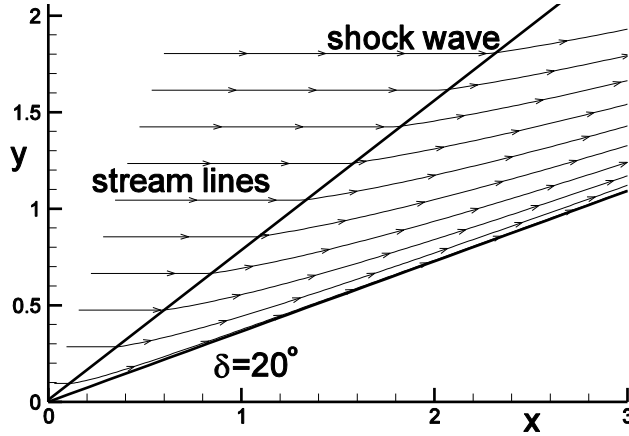cone, $\theta \simeq 37.8^o$ and $\dfrac{p_2}{p_1} \simeq 1.91$, as shown in Figure 14.57
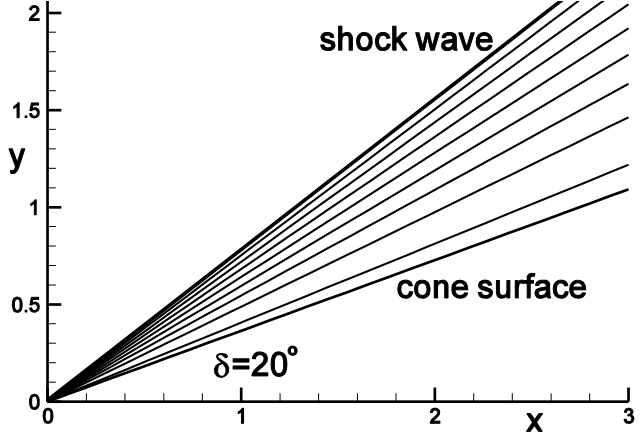

Figure 14.55 Conical flow streamlines
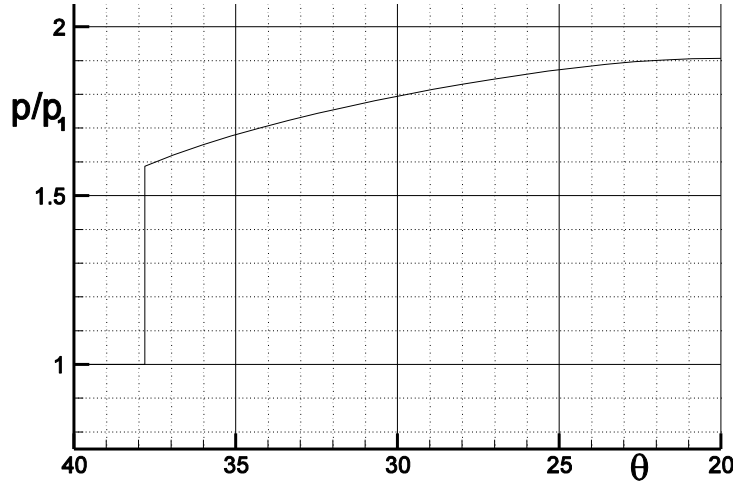

Figure 14.56 Conical flow pressure contours

Figure 14.57 Pressure vs. θ, $\theta_{shock} \simeq 37.8^o$ and $\theta_{cone} = 20^o$

The conical flow solutions shown above were obtained by integrating characteristic relations between the cone surface and an estimated shock wave ray location. The shock weave angle θ is adjusted during a relaxation procedure until the calculated pressure behind the shock wave, p_{shock}, agrees with that predicted for the shock wave angle, p_2.

$$p_{shock} \rightarrow p_2 = p_1 \frac{2\gamma M_1^2 \sin^2 \theta - (\gamma - 1)}{\gamma + 1},$$

The above relation can be obtained from the shock jump relations given earlier in Section 14.3.1. The characteristic equations are obtained from the equation for axisymmetric flow in Cartesian coordinates given at the end of Section 14.4.2, which when rewritten becomes

35

$$\frac{\partial U}{\partial t} + \frac{\partial F}{\partial x} + \frac{\partial G}{\partial y} = \frac{1}{y}\begin{bmatrix} 0 \\ 0 \\ p \\ 0 \end{bmatrix} - \frac{G}{y}$$

Using the transformations in Section 7.3, with $\xi = r$, $\eta = \theta$, as shown in Figure 14.58, $d_{xy} = r$ and the equation becomes, for steady conical flow,

$$\frac{\partial U'}{\partial t} + \frac{\partial F'}{\partial r} + \frac{\partial G'}{r\partial\theta} = \frac{1}{r\sin\theta}\left(\begin{bmatrix} 0 \\ 0 \\ p \\ 0 \end{bmatrix} - G\right) \qquad \text{with} \qquad \begin{aligned} U' &= rU \\ F' &= r\cos\theta F + r\sin\theta G \\ G' &= -\sin\theta F + \cos\theta G \end{aligned}$$
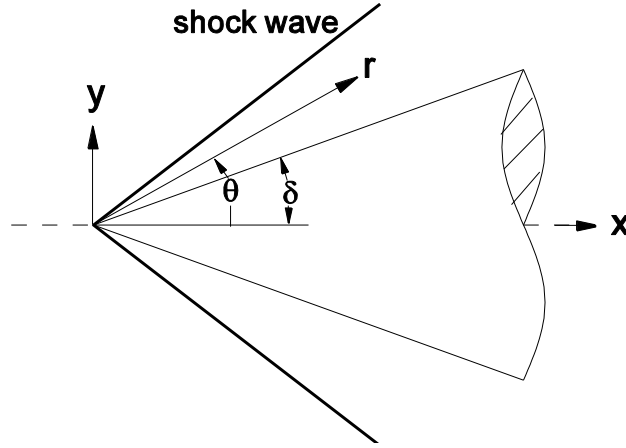
Figure 14.58 Coordinate systems $x-y$ and $r-\theta$

Note the time derivative term vanishes because the flow is steady and the derivative with respect to r vanishes because the flow is constant along rays. The equation becomes (see Characteristic Relations, Section 2.7)

$$B'\frac{\partial V}{\partial\theta} = Q \qquad \text{with } B' = \begin{bmatrix} v' & -\rho\sin\theta & \rho\cos\theta & 0 \\ 0 & v' & 0 & -\sin\theta/\rho \\ 0 & 0 & v' & \cos\theta/\rho \\ 0 & -\gamma p\sin\theta & \gamma p\cos\theta & v' \end{bmatrix}, \quad V = \begin{bmatrix} \rho \\ u \\ v \\ p \end{bmatrix}, \quad Q = -\frac{\rho v}{\sin\theta}\begin{bmatrix} 1 \\ 0 \\ 0 \\ c^2 \end{bmatrix}$$

and $v' = -\sin\theta u + \cos\theta v$. The eigenvalues of B' are $\lambda = v', v', v'+c$ and $v'-c$.

$$B' = S^{-1}\Lambda S \quad \text{with } S = \begin{bmatrix} 1 & 0 & 0 & -1/c^2 \\ 0 & \cos\theta & \sin\theta & 0 \\ 0 & -\rho c\sin\theta & \rho c\cos\theta & 1 \\ 0 & \rho c\sin\theta & -\rho c\cos\theta & 1 \end{bmatrix} \text{ and } \Lambda = \begin{bmatrix} v' & 0 & 0 & 0 \\ 0 & v' & 0 & 0 \\ 0 & 0 & v'+c & 0 \\ 0 & 0 & 0 & v'-c \end{bmatrix}$$

The four characteristic equations are, with $v' = \cos\theta\, u + \sin\theta\, v$,

(1) $\dfrac{\partial \rho}{\partial \theta} - \dfrac{1}{c^2}\dfrac{\partial p}{\partial \theta} = 0$

(2) $\dfrac{\partial u'}{\partial \theta} - v' = 0$

(3) $(v'+c)\left(\dfrac{\partial v'}{\partial \theta} + \dfrac{1}{\rho c}\dfrac{\partial p}{\partial \theta}\right) = -(v'+c)u' - \dfrac{cv}{\sin\theta}$

(4) $(v'-c)\left(\dfrac{\partial v'}{\partial \theta} - \dfrac{1}{\rho c}\dfrac{\partial p}{\partial \theta}\right) = -(v'+c)u' + \dfrac{cv}{\sin\theta}$

Equation (1) states that the flow is isentropic behind the shock wave, i.e., $p = \dfrac{p_2}{\rho_2^\gamma}\rho^\gamma$, and the second equation was used by Taylor and Maccoll to form a single equation of second degree from equations (3) and (4). The total enthalpy is also constant through the shock, $\dfrac{\gamma}{\gamma+1}\dfrac{p}{\rho} + \dfrac{u'^2+v'^2}{2} = \dfrac{\gamma}{\gamma+1}\dfrac{p_1}{\rho_1} + \dfrac{u_1^2}{2} = h$. The implicit finite difference equation to be solved is, with $\Delta\theta = \dfrac{\theta_{shock} - \delta_{cone}}{J-1}$ and $j = 1,\cdots,J$,

$$
\left\{ (v'+c)\begin{bmatrix}1 & \dfrac{1}{\rho c}\\[2mm] 0 & 0\end{bmatrix}\dfrac{D_-\cdot}{\Delta\theta} + (v'-c)\begin{bmatrix}0 & 0\\[2mm] 1 & -\dfrac{1}{\rho c}\end{bmatrix}\dfrac{D_+\cdot}{\Delta\theta} - \dfrac{\partial R^n}{\partial V_j}\right\}\delta V_j^{\,m+1} = \Delta V_j^n
$$

$$
= -\left\{ (v'+c)\begin{bmatrix}1 & \dfrac{1}{\rho c}\\[2mm] 0 & 0\end{bmatrix}\dfrac{D_-\cdot}{\Delta\theta} + (v'-c)\begin{bmatrix}0 & 0\\[2mm] 1 & -\dfrac{1}{\rho c}\end{bmatrix}\dfrac{D_+\cdot}{\Delta\theta}\right\}V_j^{\,m} + R_j^n ,
$$

with $V' = \begin{bmatrix}v'\\ p\end{bmatrix}$ and $R_j^n = -\begin{bmatrix}(v'+c)u' + \dfrac{cv}{\sin\theta}\\[2mm] (v'+c)u' - \dfrac{cv}{\sin\theta}\end{bmatrix}_j^n$

The boundary condition at the cone surface, at $j=1$, is flow tangency, $v'=0$, and at the shock wave boundary, at $j=J$, the second equation in the above set, characteristic equation (4), is replaced by the following equation, where the subscript J' indicates values just behind the shock wave previously called 2 above.

$$
(v_{J'}^m - c_{J'}^n)\left(\dfrac{-\delta v_J^m}{\Delta\theta} - \dfrac{1}{\rho c}\dfrac{-\delta p_J^n}{\Delta\theta}\right) = -(v_{J'}^m - c_{J'}^n)\left(\dfrac{v_{J'}^m - v_J^m}{\Delta\theta} - \dfrac{1}{\rho c}\dfrac{p_{J'}^n - p_J^n}{\Delta\theta}\right)
$$

where v'_2, c_2 and p_2 are the values just behind the shock wave obtained from the shock jump relations.

The implicit equation is solved by inverting the following matrix equation (see Chapter11, Section 11.2 for details).

$$
\begin{bmatrix}
A_J & C_J & 0 & 0 & 0 & 0 & 0 \\
B_{J-1} & A_{J-1} & C_{J-1} & 0 & 0 & 0 & 0 \\
0 & \ddots & \ddots & \ddots & 0 & 0 & 0 \\
0 & 0 & B_j & A_j & C_j & 0 & 0 \\
0 & 0 & 0 & \ddots & \ddots & \ddots & 0 \\
0 & 0 & 0 & 0 & B_2 & A_2 & C_2 \\
0 & 0 & 0 & 0 & 0 & B_1 & A_1
\end{bmatrix}
\begin{bmatrix}
\delta V_J^{n+1} \\
\delta V_{J-1}^{n+1} \\
\vdots \\
\delta V_j^{n+1} \\
\vdots \\
\delta V_2^{n+1} \\
\delta V_1^{n+1}
\end{bmatrix}
=
\begin{bmatrix}
\Delta V_J^n \\
\Delta V_{J-1}^n \\
\vdots \\
\Delta V_j^n \\
\vdots \\
\Delta V_2^n \\
\Delta V_1^n
\end{bmatrix}
$$

where for $j = 2, \cdots, J-1$

$$
B_j = \frac{(v'-c)_{j+1/2}^n}{\Delta\theta}
\begin{bmatrix}
0 & 0 \\
1 & \dfrac{-1}{\rho c}
\end{bmatrix}_{j+1/2}^n
, \quad
C_j = -\frac{(v'+c)_{j-1/2}^n}{\Delta\theta}
\begin{bmatrix}
1 & \dfrac{1}{\rho c} \\
0 & 0
\end{bmatrix}_{j-1/2}^n
\quad \text{and} \quad A_j = -B_j - C_j
$$

At the cone surface boundary

$$
B_1 = \frac{-c_{1+1/2}^n}{\Delta\theta}
\begin{bmatrix}
0 & 0 \\
1 & \dfrac{-1}{\rho c}
\end{bmatrix}_{1+1/2}^n
, \quad
A_1 =
\begin{bmatrix}
1 & 0 \\
1 & \dfrac{-1}{\rho \Delta\theta}
\end{bmatrix}_{1+1/2}^n
\quad \text{and} \quad
\Delta V_1^n =
\begin{bmatrix}
0 \\
c\left(\dfrac{v_2^n}{\Delta\theta} - \dfrac{p_2^n - p_1^2}{\rho c\Delta\theta}\right) + \left(cu' - \dfrac{cv}{\sin\theta}\right)_{1+1/2}^n
\end{bmatrix}
$$

At the shock wave surface boundary

$$
C_J = -\frac{(v'+c)_{J-1/2}^n}{\Delta\theta}
\begin{bmatrix}
1 & \dfrac{1}{\rho c} \\
0 & 0
\end{bmatrix}_{J-1/2}^n
, \quad
A_J = -\frac{(v''_{J'} - c_{J'}^n)}{\Delta\theta}
\begin{bmatrix}
0 & 0 \\
1 & \dfrac{-1}{\rho c}
\end{bmatrix}_{J'}^n - C_J \quad \text{and}
$$

$$
\Delta V_1^n =
\begin{bmatrix}
(v''_{J-1/2} + c_{J-1/2}^n)\left(\dfrac{v''_J - v''_{J-1}}{\Delta\theta} + \dfrac{p_J^n - p_{J-1}^n}{\rho c\Delta\theta}\right) + \left((v'+c)u' + \dfrac{cv}{\sin\theta}\right)_{J-1/2}^n \\
(v''_{J'} - c_{J'}^n)\left(\dfrac{v_{J'}^n - v''_J}{\Delta\theta} - \dfrac{p_{J'}^n - p_J^n}{\rho c\Delta\theta}\right)
\end{bmatrix}
$$

The above matrix is solved iteratively for $n = 1, 2, \cdots, N$ until

$$
p_J^n \rightarrow p_{J'}^n = p_1 \frac{2\gamma M_1^2 \sin^2\theta_{shock}^n - (\gamma-1)}{\gamma+1}.
$$ After each iteration θ_{shock}^n is reset according to

$$\theta_{shock}^{n+1} = \sin^{-1}\left(\frac{1}{2\gamma M_1^2}\left(\frac{p_J^n}{p_1}(\gamma+1)+\gamma-1\right)\right)$$

Near the limits for large δ_{cone} a relaxation for $\theta_{shock}^{n+1} \leftarrow \varpi\theta_{shock}^{n+1} + (1-\varpi)\theta_{shock}^{n}$, with $0 < \varpi \le 1$ may improve convergence. Values of $N = 25$ should be more than sufficient.

Figures 14.59-61 show graphs of shock wave angle versus cone half angle, $\theta \, vs. \, \delta$, and the surface pressure to free stream pressure ratio versus cone half angle, $\dfrac{p_{cone}}{p_\infty} \, vs. \, \delta$, for a few free stream Mach number curves, from $M_\infty = 1.25 \, to \, 6$.
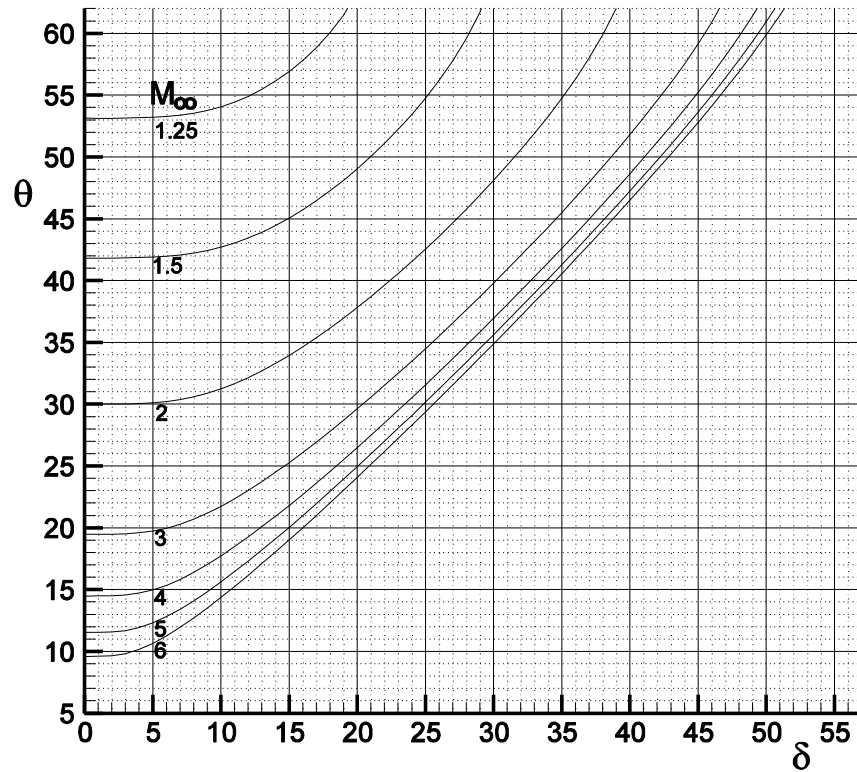
Figure 14.59 Shock wave angle versus cone half angle, $\theta \, vs. \, \delta$, for M_∞ curves
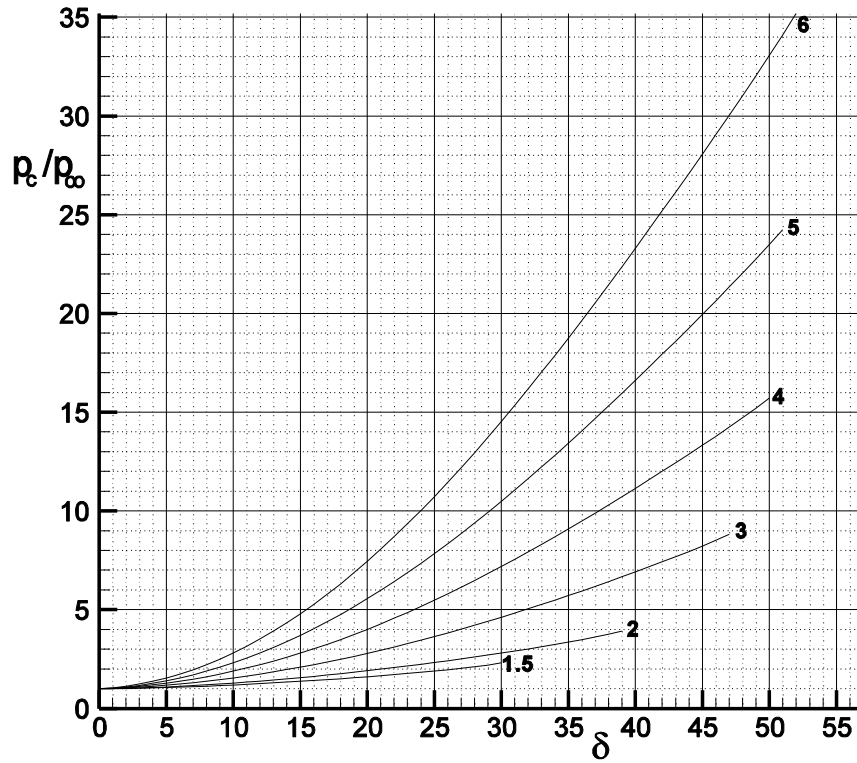
Figure 14.60 Surface pressure to free stream pressure ratio, $\dfrac{p_{cone}}{p_\infty}$ $vs.\,\delta$, for M_∞ curves
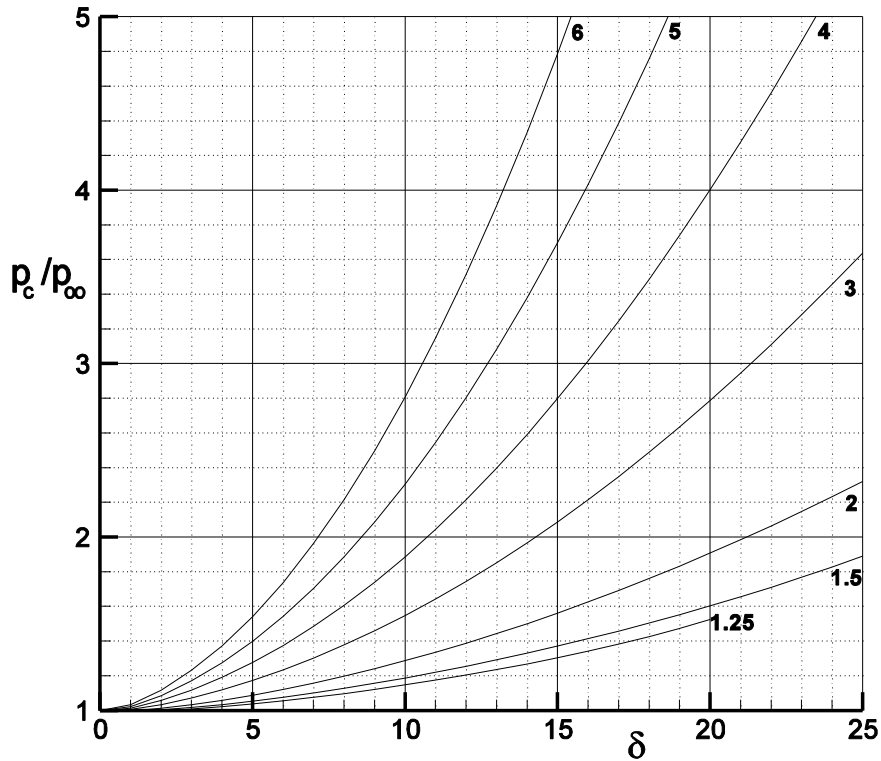
Figure 14.61 Detail for small values of $\dfrac{p_{cone}}{p_\infty}$ $vs.\,\delta$, for M_∞ curves

The above algorithm solves for flow past slender cones whose shock waves are attached to the cone. It is not suitable for detached shock waves, cones at angle of attack or bodies deviating from that of a cone. The next section presents a general method, without these restrictions, applied also to flow past a cone.

14.5 Axisymmetric Applications
14.5.1 Application: Flow Past a Cone

Exercise(4): Modify the wedge flow program of Section 14.3.1 to solve the two dimensional axisymmetric Euler equations for Mach 2 flow past a cone with half cone angle $\delta = 20^o$. Use the same initial and boundary conditions for the flow sketched in Figure 14.3 and the Case (1) and (2) meshes with any numerical method described in Chap. 9. Note that this flow will be non-conical downstream of the apex of the cone because of the solid wall at the top boundary.

Cone Solutions:
Run your program until convergence, about 250 time steps.
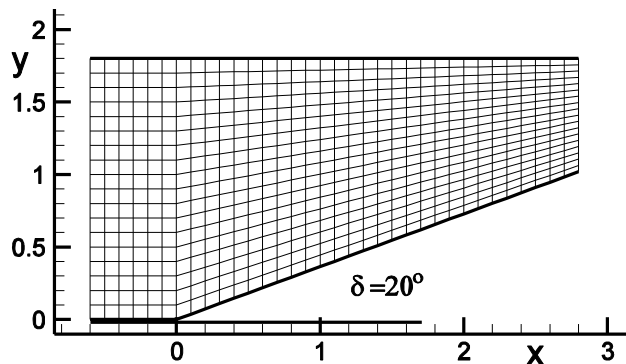
Figure 14.62 Case (1) Mesh
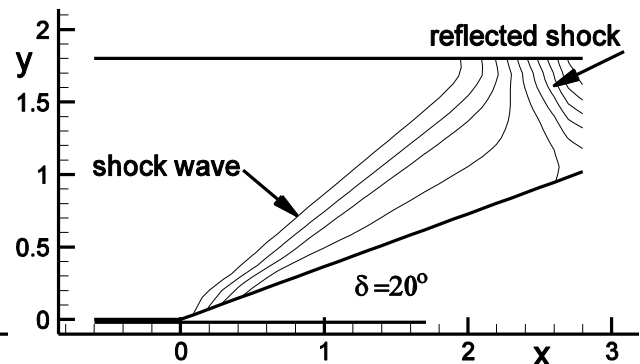
Figure 14.63 Pressure contours, Mod S-W method
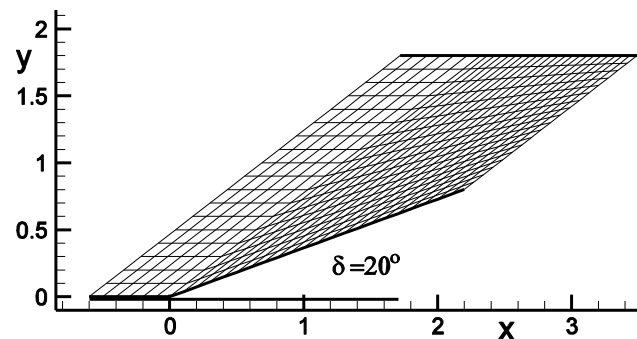
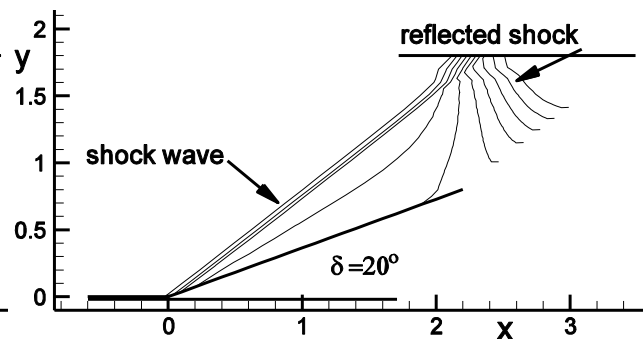**Figure 14.64** Case (2) Swept mesh

Figure 14.65 Pressure contours, Roe method

The exact and computed surface pressures are compared for both meshes below, through shock wave (along j=2), for both the MacCormack method and the first order accurate Roe method for $\delta = 20^o$.
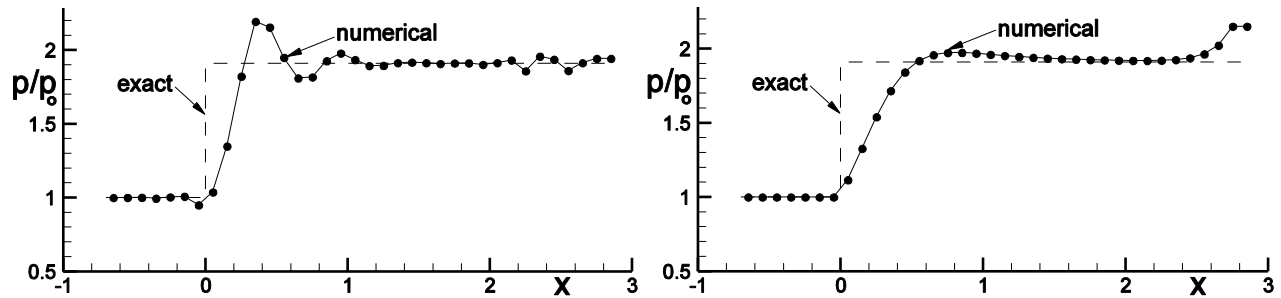
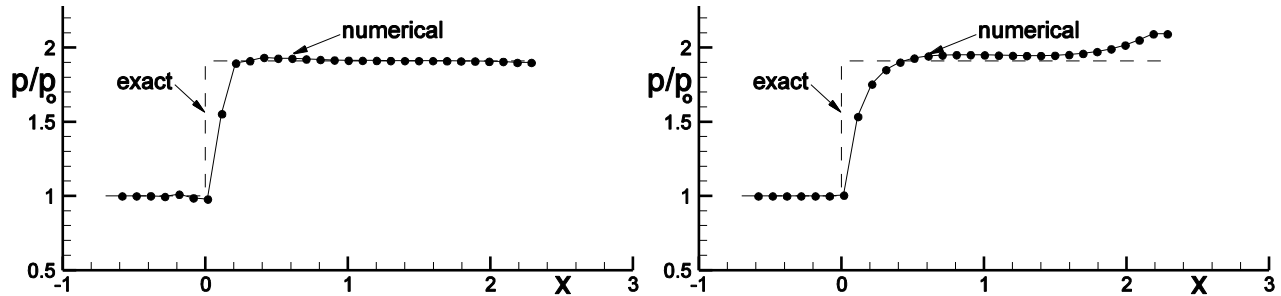**Figure 14.66** Mesh Case (1) results, pressure, at left MacCormack method and at right Roe method

Figure 14.67 Mesh Case (2) results, pressure, at left MacCormack method and at right Roe method

The rise in pressure near the exit for the Roe method is caused by the pressure gradient from the reflected shock wave from the top wall and the choice of only first order accuracy, which excessively spreads the pressure gradient to the cone surface. The oscillation of the MacCormack method at the bow shock wave is caused by second order methods representing "step" discontinuities with a finite spectrum of Fourier components, the so called Gibbs phenomena. The oscillation near the exit may be waves excited by the shock oscillation being partially reflected by the exit boundary conditions.

The Case (1) mesh results are disappointing, particularly for the formation of the shock wave. This was caused by too few mesh points in the y-direction near the cone apex to resolve the start of the shock wave. The solution procedure of the conical flow Section 14.4.3 could be used to calculate the flow near the cone apex to provide the entrance boundary condition for the flow downstream of apex. Alternatively, the present solution method could itself be used, with the top wall boundary moved far above to avoid reflection back into the flow about the cone. This solution could then be transformed back to that near the cone apex, taking advantage of the lack of a reference length for conical flow. This procedure is known as the "step back" procedure for generating a starting solution for flows past conically pointed body shapes.
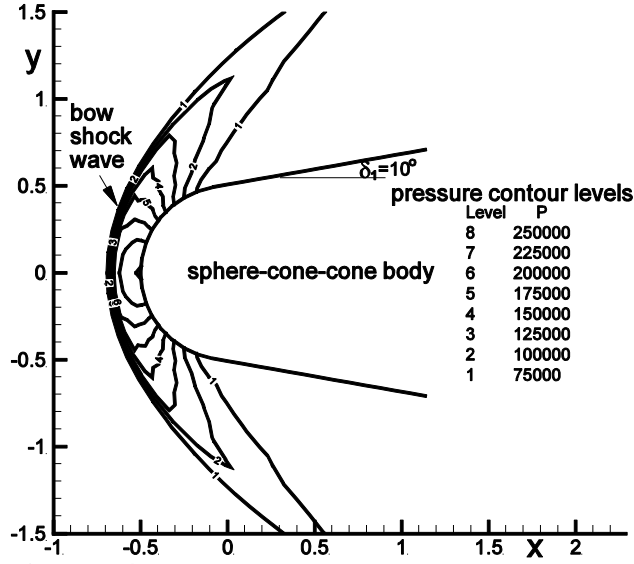
14.5.2 Flow Past a Blunt Body

42

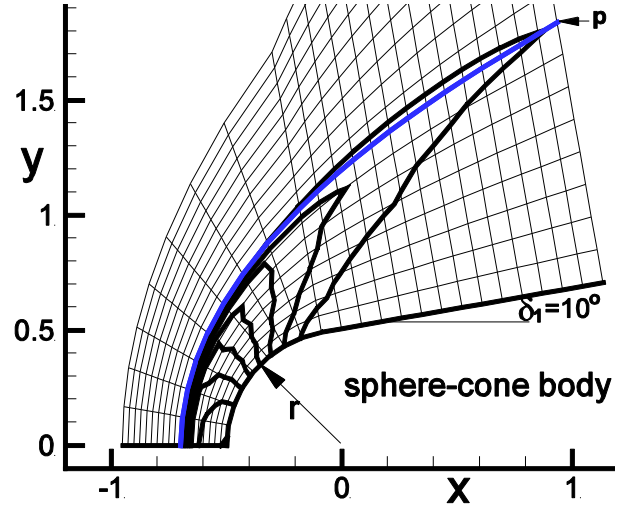**Figure 14.68** Pressure contours, sphere-cone body   **Figure 14.69** Mesh with pressure contours

Figures 14.68 and 14.69 show the pressure contours and mesh for axisymmetric flow past a sphere-cone body. The half cone angle is $\delta = 10^o$ and the radius of the sphere is $r = 0.5m$. The cone joins the surface of the sphere tangentially at $\theta = 90^o - \delta$, measured from the axis of symmetry. The origin of the coordinate system is at the sphere center. The freestream $p_\infty = 4.563 \times 10^4 N/m^2$ and $T_\infty = 300^o K$.

Exercise(5): Modify your axisymmetric flow program of the previous section to solve the Euler equations for supersonic flow past a sphere-cone body. Use a free stream Mach number $M_\infty = 2$ and a half cone angle $\delta = 10^o$. Solve with any explicit numerical method described in Chapter 9.

Mesh
The mesh line $\eta = 2 - 1/2$ lies along the body surface and a line of the mesh, $\eta = j_{shock} - 1/2$, is set to be aligned with the shock wave near the nose of the body, using the shape of a parabola. Two points are chosen to set the equation for the parabola, the shock standoff distance, sd, and a point along the shock wave at $x = 0$. They are given by $(-r - sd, 0)$ and $(0, y_{shock})$. Reasonable choices can be found by trial and error. The values used for the above results were $(-0.7, 0)$ and $(0, 1.2)$. The parabola, shown as gridline marked **p** in Figure 14.69, is given by

$$x = x_0 + ay^2, \quad \text{where} \quad x_0 = -r - sd \quad \text{and} \quad a = \frac{-x_0}{y_{shock}^2}$$

Mesh points are spaced equally along the sphere surface from $\theta = 0$ to $\theta = 90^o - \delta$, $i = 2$ *to* i_{scj}.

$$\begin{aligned} x_{i-1/2, 2-1/2} &= -r\cos\theta_{i-1/2} \\ y_{i-1/2, 2-1/2} &= r\sin\theta_{i-1/2} \end{aligned}, \quad \text{where } \theta_{i-1/2} = (i-2)\Delta\theta \text{ and } \Delta\theta = \frac{90^0 - \delta}{i_{scj} - 2}$$

Mesh points are spaced equally along the cone surface with $\Delta x = r\Delta\theta$, $i = i_{scj} + 1$ to IL

$$x_{i-1/2,2-1/2} = x_{i_{scj}-1/2,2-1/2} + (i-i_{scj})\Delta x$$

$$y_{i-1/2,2-1/2} = y_{i_{scj}-1/2,2-1/2} + (i-i_{scj})\Delta x \tan\delta$$

For the results shown in the above figures, the sphere-cone-junction index $i_{scj} = 10$ and $IL = 24$. The lines $\xi = i - 1/2$ for $i = 2$ to i_{scj} are radial and equally spaced from the body to the parabola representing the shock wave. If the intersection of the radial line $\xi = i - 1/2$ with the parabola is given by (x_{par}, y_{par}), then for $j = 2$ to JL

$$x_{i-1/2,j-1/2} = x_{i-1/2,2-1/2} + (j-2)\Delta x'$$
$$y_{i-1/2,j-1/2} = y_{i-1/2,2-1/2} + (j-2)\Delta y'$$, where $\Delta x' = \dfrac{x_{par} - x_{i-1/2,2-1/2}}{j_{shock} - 2}$ and $\Delta y' = \dfrac{y_{par} - y_{i-1/2,2-1/2}}{j_{shock} - 2}$

For the present calculations $j_{shock} = 10$ and $JL = 20$. The lines $\xi = i - 1/2$ for $i = i_{scj} + 1$ to IL are lines normal to the body, which also intersect the parabola. However, if the slope of the parabola, $\dfrac{dy}{dx} = \dfrac{1}{2ay}$, becomes less than the tangent of the shock wave angle for the cone, in our Mach 2 case $\theta_{shock} \simeq 31.3^o$, then, instead of the curve for the parabola, a straight line extension with slope $\tan\theta_{shock}$ should be used. This may occur near the exit of the mesh.

Initial Conditions

Set the flow variables to their free stream values outside of the parabola, for all mesh points with $j \geq j_{shock}$. For each mesh point i, j, with $j < j_{shock}$ use the solution of the shock jump relations (shown earlier in the section on the flow past a wedge) to set the initial values behind the shock wave. The following quadratic equation for u_2' with θ obtained from the tangent to the parabola is solved for each mesh point i along the mesh line representing the parabola approximating the initial shock wave.
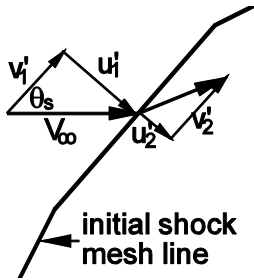

$$f(\theta_{s_i}) = \frac{\gamma}{\gamma - 1}\frac{n}{m}u_2' + \left(\frac{1}{2} - \frac{\gamma}{\gamma - 1}\right)u_2'^2 + \frac{1}{2}v_1'^2 - h = 0$$

with

$$\theta_{s_i} = \tan^{-1}\left(\frac{y_{i+1/2, j_{shock}-1/2} - y_{i-1/2, j_{shock}-1/2}}{x_{i+1/2, j_{shock}-1/2} - x_{i-1/2, j_{shock}-1/2}}\right)$$

Figure 14.70 Shock wave velocity components

After solving for u_2', the jump relations given earlier can be used to find ρ_2, v_2' and p_2. The Cartesian velocity components u_2 and v_2 at the shock wave are given by

$$\begin{bmatrix} u_2 \\ v_2 \end{bmatrix} = \begin{bmatrix} \sin\theta_s & \cos\theta_s \\ -\cos\theta_s & \sin\theta_s \end{bmatrix} \begin{bmatrix} u_2' \\ v_2' \end{bmatrix}$$

The velocity component normal to the wall should go to zero as the wall is approached, as j decreases, to satisfy the flow tangency condition at the wall surface. Now let u''_{shock} and v''_{shock} be the components of the velocity at the shock wave that are in the direction parallel and normal to the wall, respectively.

$$\begin{bmatrix} u''_{shock} \\ v''_{shock} \end{bmatrix} = \begin{bmatrix} \cos\theta_w & \sin\theta_w \\ -\sin w_w & \cos\theta_w \end{bmatrix} \begin{bmatrix} u_2 \\ v_2 \end{bmatrix}$$
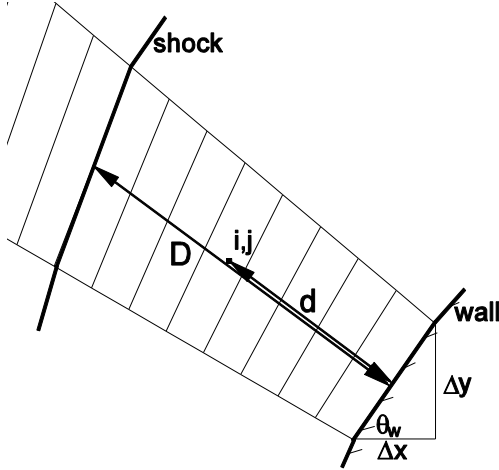
Figure 14.71 Column i of mesh

Then $u_{i,j}$ and $v_{i,j}$ are set within the column "i" of the mesh, for all j between the shock and the wall, by

$$\begin{bmatrix} u_{i,j} \\ v_{i,j} \end{bmatrix} = \begin{bmatrix} \cos\theta_w & -\sin\theta_w \\ \sin w_w & \cos\theta_w \end{bmatrix} \begin{bmatrix} u''_{shock} \\ v''_{shock} \dfrac{d}{D} \end{bmatrix}$$

Where d is the distance of the mesh point to the wall, D is the distance from the wall to the shock wave and $\theta_w = \tan^{-1}(\Delta y / \Delta x)$, as shown in the figure to the left.

Boundary Conditions
The far field boundary conditions at $j = JL$ are fixed at the uniform free stream values. Along the body surface, at $j = 2-1/2$, the same solid wall boundary conditions used for the wedge are imposed. Similarly, the exit, at $i = IL$, uses the same boundary conditions as previously for flow past the wedge. Along the axis of symmetry, $i = 2-1/2$, the surface area vanishes and the flux should be simply set to zero, $F'_{2-1/2,j} = [0]$. This axis of symmetry boundary condition will be changed in Chapter 17 for viscous flow.

Sphere-Cone Solutions
Run your program until convergence, about 500 time steps.

The results shown in Figures 14.72 and 14.73 used the MacCormack method. The results for the Modified Steger-Warming and Roe methods are shown in Figures 14.74 to 14.77. The maximum pressure ratio just behind the shock wave should be $\dfrac{p_{shock}}{p_\infty} = 4.50$ and at the stagnation point

$$\dfrac{p_{stag}}{p_\infty} \simeq 5.29.$$
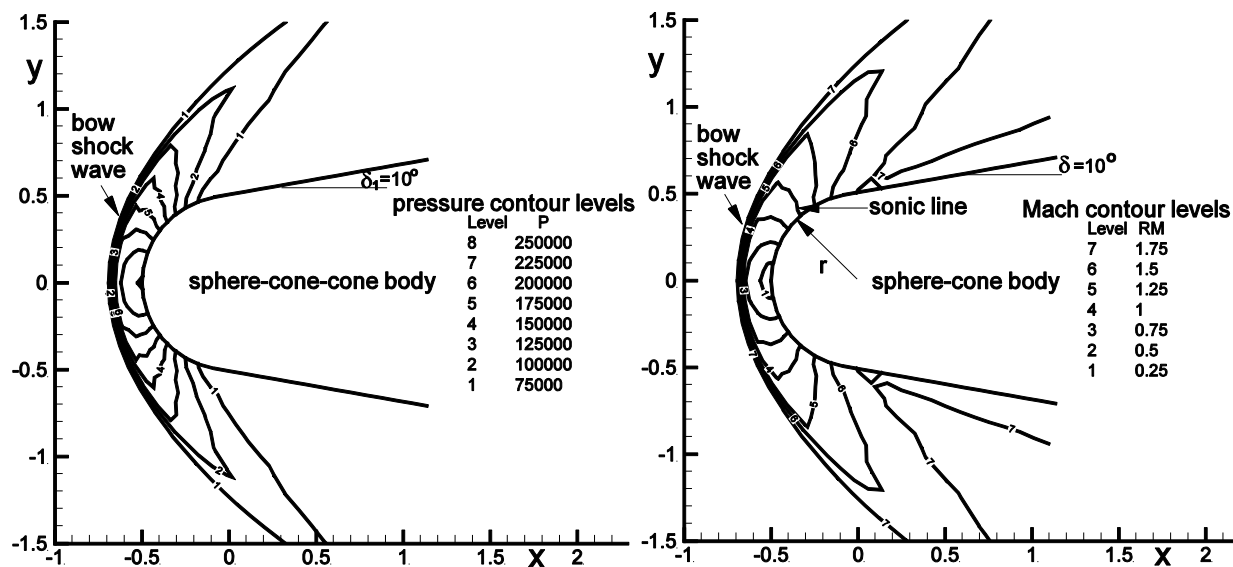
45

Figure 14.72 Mach and pressure contours, sphere-cone body
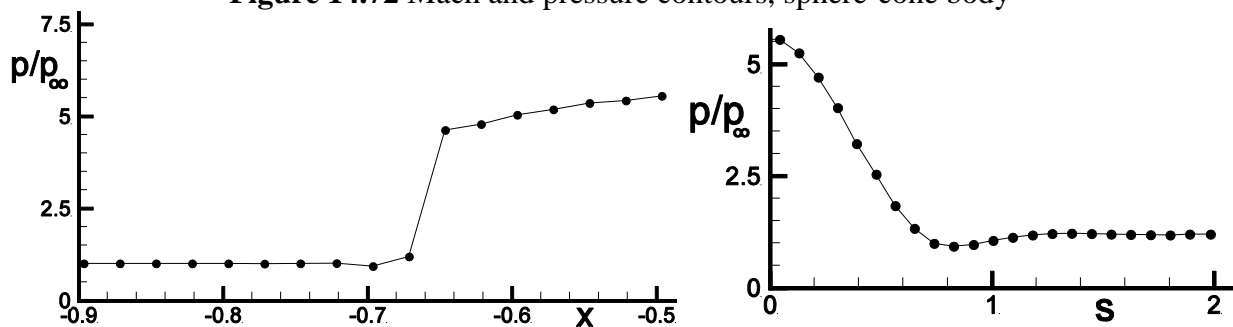

Figure 14.73 Pressure along stagnation streamline,   Pressure along sphere-cone surface
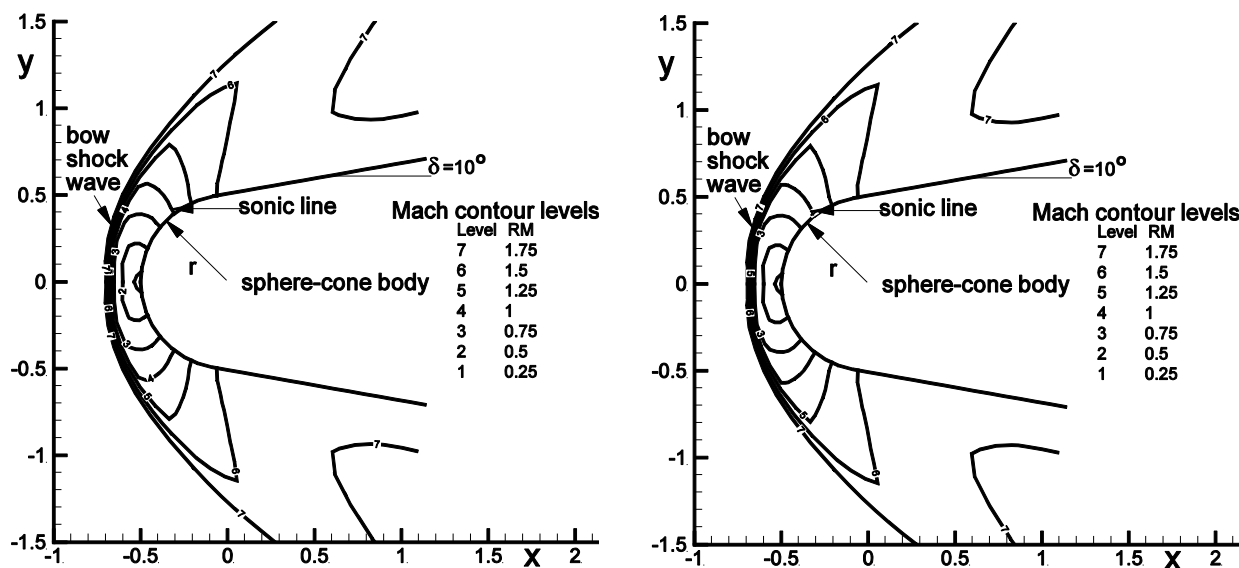

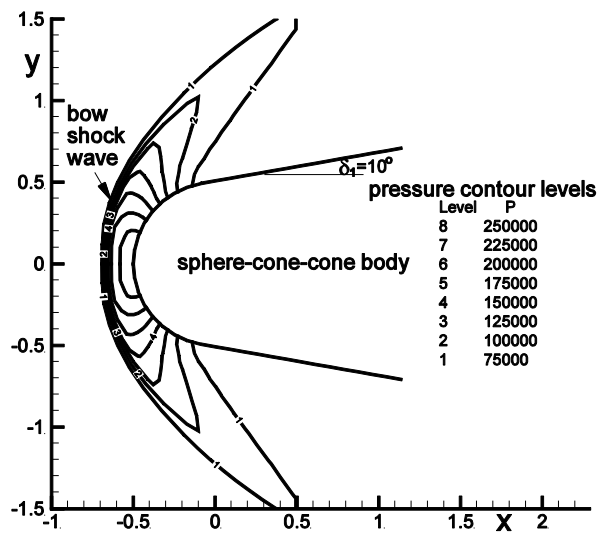**Figure 14.74** Mach contours, Mod-S-W method   Mach contours, Roe method
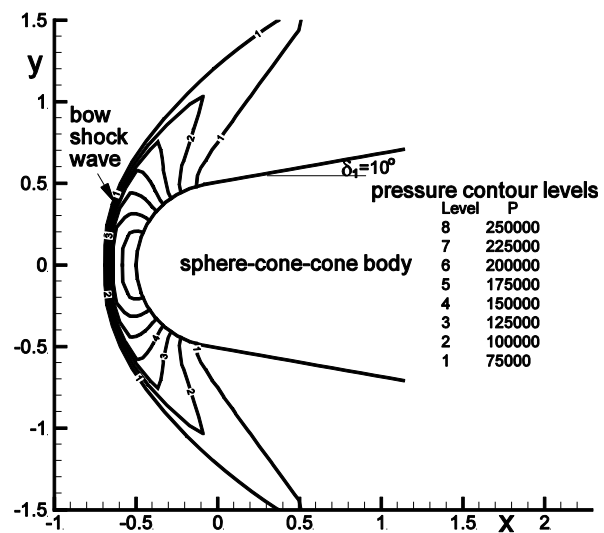
Figure 14.75 Pressure contours, Mod-S-W method,   Pressure contours, Roe method
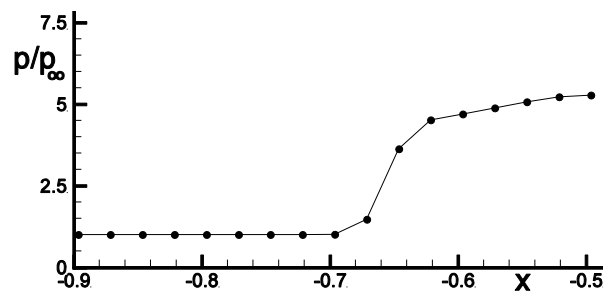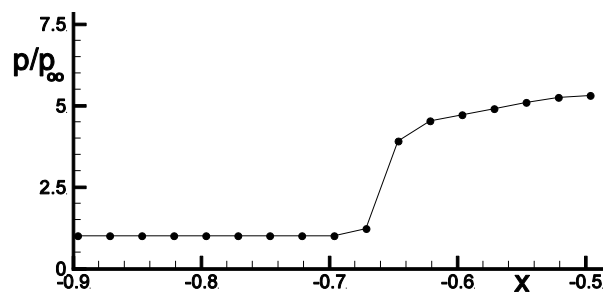

Figure 14.76 Stagnation line pressure, Mod-S-W   Stagnation line pressure, Roe
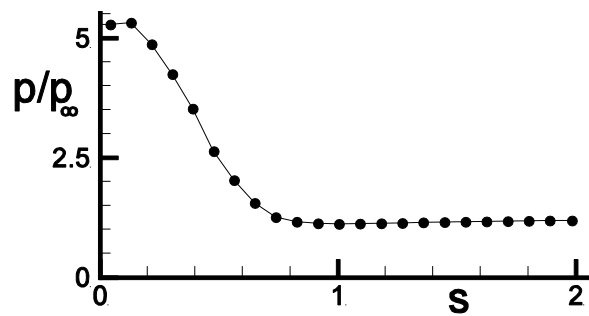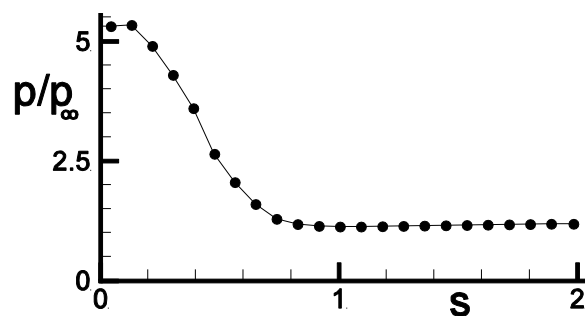

Figure 14.77 Surface pressure, Mod-S-W,   Surface pressure, Roe method